NIST

United States Department of Commerce
Technology Administration
National Institute of Standards and Technology

NISTIR 5004

CRYOGENIC MECHANICAL TESTING OF AL-LI ALLOYS AT NIST

P.T. Purtscher

CRYOGENIC MECHANICAL TESTING OF AL-LI ALLOYS AT NIST

P.T. Purtscher

Materials Reliability Division
Materials Science and Engineering Laboratory
National Institute of Standards and Technology
Boulder, Colorado 80303-3328

TABLES OF CONTENTS

CRYOGENIC MECHANICAL TESTING OF AL-LI ALLOYS AT NIST

Patrick T. Purtscher
National Institute of Standards and Technology

SUMMARY

Work done in 1992 at NIST in support of the National Launch System (NLS) program consisted of two parts. The first part (Part A) was an evaluation of Al-Cu-Li-Mg-Ag-Zr alloys to determine whether recent developments in the relatively new alloy produced significant improvements in the tensile and fracture toughness. The results show that there is only a slight difference between the mechanical properties of the three variations of Al-Cu-Li-Mg-Ag-Zr alloys from room temperature down to liquid-helium temperature. All three show an increase at cryogenic temperatures in the tensile flow and fracture stresses, all orientations, and fracture toughness in L-T orientation only over the values at room temperature. Fracture toughness for the S-L orientation decreases with decreasing test temperature, and no consistent trend is observed for fracture toughness in the T-L orientation. We observe a correlation between the tensile flow and fracture properties and fracture toughness in the short transverse orientation, where the fracture appearance of tensile and toughness specimens are similar.

The second part (Part B) of our program evaluated the effect of product form on the residual strength and mechanical behavior of Alloy 2090 between room and liquid-helium temperature. Three different product forms were included in the program: sheets, extrusions, and welds. At room temperature, sheets that exhibited delaminations on the fracture surface had the highest defect tolerance of the three product forms tested. In addition, the sheets with delaminations demonstrated the largest increase in residual strength with decreasing test temperature of any of the product forms tested here. The superior performance of sheets is attributed to the formation of delaminations on the fracture surface during the overload testing.

key words: aluminum-lithium alloys, cryogenic mechanical properties, delaminations, extrusions, fracture toughness, sheets, surface-cracked panels, welds

PART A

CRYOGENIC MECHANICAL PROPERTIES OF Al-Cu-Li-Mg-Ag-Zr ALLOYS

P.T. Purtscher and B.T. Pham[1]

INTRODUCTION

Strong aluminum-lithium (Al-Li) alloys offer a significant cost-saving potential for application to advanced launch and space vehicles. The high specific strength and stiffness of Al-Li alloys has brought the initial attention to these materials [A1]. The development of these alloys depends upon better characterization of the relationship between processing, microstructure, and properties.

The Al-Cu-Li-Mg-Ag-Zr system was developed to maximize the strength and still maintain good resistance to hot cracking after welding [A2-A4]. Within the Al-Cu-Li-Mg-Ag-Zr system, Alloys 2094 and 2095 offer the highest strength of any commercially available Al-Li alloys and are prime candidates for any new aerospace application.

A significant requirement in many aerospace designs is the ratio of yield strength (YS) and fracture toughness (K_{Ic}) at cryogenic temperature (CT) compared to that at room temperature (RT) [A2]. If the mechanical properties improve at CT compared to RT, i.e., ratios

$$\frac{YS @ CT}{YS @ RT} \text{ and } \frac{K_{Ic} @ CT}{K_{Ic} @ RT} > 1 \qquad (1)$$

then the structures can be proof tested at RT to insure safe operation at the CT of interest. If the ratios are less than 1, then the design stress will have to be lowered, and the potential saving offered by Al-Li alloys will be minimized.

---

[1]Formerly at Phillips Laboratory, Edwards Air Force Base, CA; currently at the Missile and Space Command, Los Angeles Air Force Base, CA.

2

Our purpose in this study is to look at different commercial alloys within the Al-Cu-Li-Mg-Ag-Zr system. Changes in composition and processing will affect the weldability, density, stiffness, strength, and toughness of the material. The goal here is to measure the cryogenic mechanical properties of the existing commercial alloys that are available and to study the mechanisms responsible for those properties.

MATERIALS

Three variations in chemical composition within the base alloy system were tested and are shown in **Table A1**. Lot 1 with the highest Li and Cu content fits into the 2094 composition range and Lot 3 fits into the range for 2095. Lot 2 corresponds to the overlap in allowables for the two alloys.

Table A1. Compositions of Al-Li Alloys, mass %.

Alloy	Cu	Li	Mg	Zr	Si	Fe	Ag	Ti
Lot 1	4.72	1.28	0.42	0.12	0.02	0.03	0.35	0.02
Lot 2	4.36	1.25	0.39	0.14	0.03	0.07	0.35	0.02
Lot 3	4.08	1.01	0.35	0.13	0.03	0.03	0.35	0.03

The starting materials were in the form plates 13 mm thick. The heat treatment schedules for all the plates were similar in that they were first solution-treated, then quenched, mechanically stretched, and artificially aged to a slightly underaged condition by the producer. The temper designation is RT70.

PROCEDURES

Tensile tests were run in three environments and temperatures (room air at 295 K, liquid nitrogen (LN2) at 76 K, and liquid helium (LHe) at 4 K). For the long-transverse and longitudinal orientations, the gage section of the tensile specimens was 6.25 mm in diameter and 33 mm in length. Duplicate tests were run on specimens from lots 1 and 2 while triplicate tests were performed on lot 3. Tensile tests were conducted in a screw-driven test machine with a 100 kN load capacity. Cross-head rate for testing was 0.5 mm/min, which translates to an initial elastic strain rate of 2.5×10^{-4}. YS, ultimate tensile strength (UTS), and fracture stresses were calculated for each test. The uniform strain was determined by the change in cross section in the gage length away from the fracture. The ductility of the alloys

was determined with measurements of the changes in gage length (% El.) and cross sectional area (% RA). The elastic properties for these three alloys and the tensile properties for the first two alloys were previously reported [A5,A6].

The tensile tests in the short-transverse orientation were performed on specimens from lots 1 and 3. The ultimate tensile strength and % RA were measured from a specimen with an hourglass-shaped gage section, 7.1 mm long and 2.1 mm minimum diameter. The yield strength and % El could not be measured reliably with the nonstandard specimen.

The precision associated with the results of tensile testing is discussed elsewhere [7]. The precision of the measurements for stress reported here is estimated to be about ±1%. Measurement of ductility is less precise, about ±5%.

The tensile fracture stresses were evaluated according to a procedure used previously to characterize the effect of different metallurgical variables on the tensile fracture of steel [A8-A11]. Past experience has shown that the interfacial stress σ_{rr} initially defined by Argon et al. [A12] is a valuable measure of how metallurgical variables influence fracture in tension (σ_{rr} is approximately equal to the sum of the equivalent plastic flow stress σ_0 and hydrostatic stress σ_T). The analysis of interfacial stress can be applied at any point on the stress-strain curve of a tension test. At the point of fracture, the analysis is taken as a measure of fracture resistance.

Figure A1 shows how the measurements were made on a broken tensile specimen. The ratio of a/R is a measure of the stress concentration in the neck at the point of tensile fracture. **Equations. (A1) and (A2)** define the stresses relevant to fracture of a round, uniaxial tensile specimen [A13]:

$$\sigma_z / \sigma_0 = 1 / \{[1 + (2R/a)][\ln(1 + (a/2R))]\}, \qquad (A1)$$

where σ_z is the fracture stress, σ_0 is the equivalent plastic flow stress, R is the radius of curvature along the tensile axis of the specimen, and a is measured at the minimum cross section of the specimen.

$$\sigma_T / \sigma_0 = 1/3 + \ln (1 + (a/2R) - (r^2 /2aR)), \qquad (A2)$$

where σ_T is the hydrostatic stress at an isolated second-phase particle in a deforming matrix.

Toughness tests were run according to ASTM E 1304 with short-bar specimens, 12.7 mm thick and 25.4 mm long (W/B = 2.0). The toughness measured in ASTM E 1304 is referred to as K_{Iv}, and is similar, but not identical to the parameter K_{Ic} that is measured in ASTM E
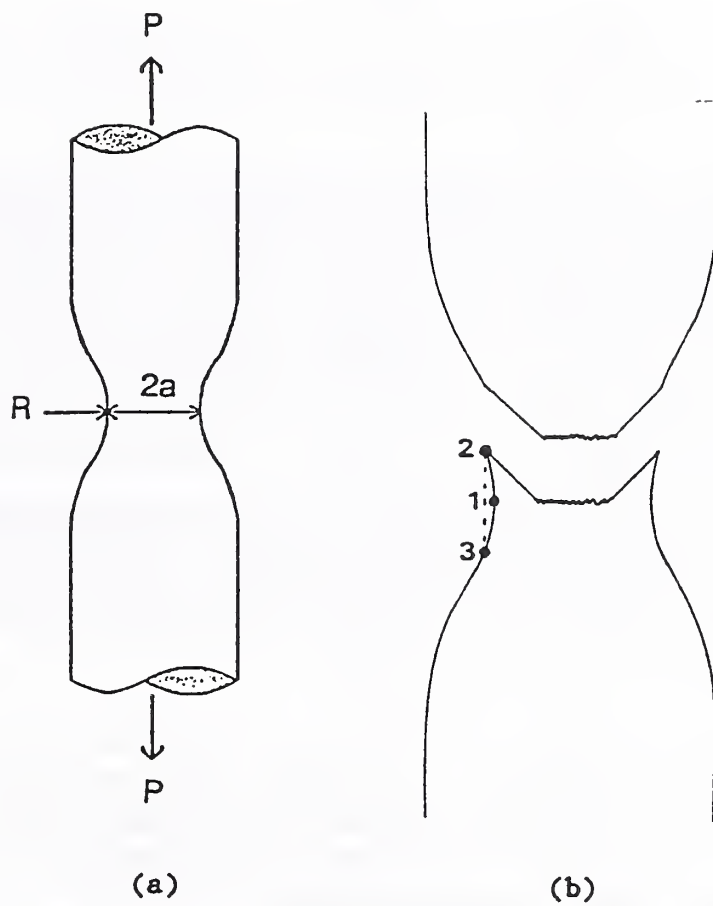
Fig. A1.   Schematic diagram that demonstrates the procedure for measurement of the parameters *a* and *R*.   (a) Definition of parameters and (b) location of the three points needed to calculate *R*.

399. The tests were run on a servo-hydraulically controlled test machine with a 100 kN load capacity. Previous data for short-bar specimens with W/B = 1.45 and compact specimens tested according to ASTM E 813 were reported elsewhere [A14].

The precision associated with fracture toughness measurements has been discussed elsewhere [A15]. For the toughness measurements reported in this paper, the precision is estimated to be ±4%.

The fracture surfaces of selected specimens were examined in a scanning electron microscope. The primary failure modes were documented and related to the failure mechanisms.

RESULTS

Mechanical tests:

Table A2 is a summary of the tensile flow stresses and ductilities as a function of temperature and composition. Figure A2 is a plot of the temperature dependence of the flow stresses. All three alloys had a similar temperature dependence. Figures A3 and A4 show engineering stress-vs.-strain curves for representative specimens from Lot 1 in long-transverse and longitudinal orientations at RT and at 76 K. At RT, the curves go through a maximum and then decrease before failure. In LN2, failure occurs near maximum load.

The strain hardening during tensile testing is similar for all lots. The uniform strain measured from the specimens, see Table A2, shows a slight increase with decreasing temperature in the longitudinal orientation. In the long-transverse orientation, the change in uniform strain with test temperature is inconsistent.

Table A3 is a summary of the tensile fracture data calculated from Eqs. (A1) and (A2) as a function of temperature and lot. The fracture stress increases for each alloy and orientation with decreasing temperature, and the critical interfacial stress usually shows the same trend. However, the ratio of the interfacial stress at fracture to UTS is always lower at cryogenic temperatures than at room temperature.

Table A4 summarizes the toughness results. The L-T specimens tested below RT demonstrate significant out-of-plane cracking. Frequently, crack jumps were encountered in testing; those cases where the load drop was greater than 5% of the maximum load are noted in Table A4.

6

Table A2.   Summary of tensile flow stresses and ductilites.

Temperature, orientation	Young's modulus,[*] GPa (msi)	YS, MPa (ksi)	UTS, MPa (ksi)	Uniform strain	% El	% RA
LOT 1						
295 K, T		581 (84)	638 (92)	0.027	11	22
L	76.5 (11.1)	607 (88)	640 (93)	0.029	10	20
S		---	627 (91)	--	--	
76 K, T		677 (98)	761 (110)	0.036	9	12
L	84.3 (12.2)	712 (103)	782 (113)	0.040	11	14
S		---	745 (108)	--	--	
4 K, T		744 (108)	859 (124)	0.031	8	10
L	85 (12.3)	785 (114)	893 (129)	0.052	11	13
S		---	812 (118)	--	--	
LOT 2						
295 K, T	76.3 (11.1)	590 (86)	633 (92)	0.021	10	27
L		615 (89)	644 (93)	0.022	10	23
76 K, T	84.1 (12.2)	680 (99)	760 (110)	0.027	9	15
L		717 (104)	782 (113)	0.032	9	17
4 K, T	84.9 (12.3)	775 (112)	853 (124)	0.027	9	14
L		780 (113)	884 (128)	0.035	10	12
LOT 3						
295 K, T		563 (82)	585 (85)	0.017	7	12
L	75.3 (10.9)	574 (83)	597 (87)	0.022	7	15
S		---	631 (91)	--	--	
76 K, T		657 (95)	712 (103)	0.023	6	6
L	83.0 (12.0)	690 (100)	743 (108)	0.030	7	8
S		---	748 (108)	--	--	
4 K, T		732 (106)	807 (117)	0.026	6	6
L	83.7 (12.1)	743 (108)	848 (123)	0.036	10	8
S		---	777 (113)	--	--	

[*]   Measured with ultasonic technique, previously reported in Ref. A6. Represents the average for the three orientations.
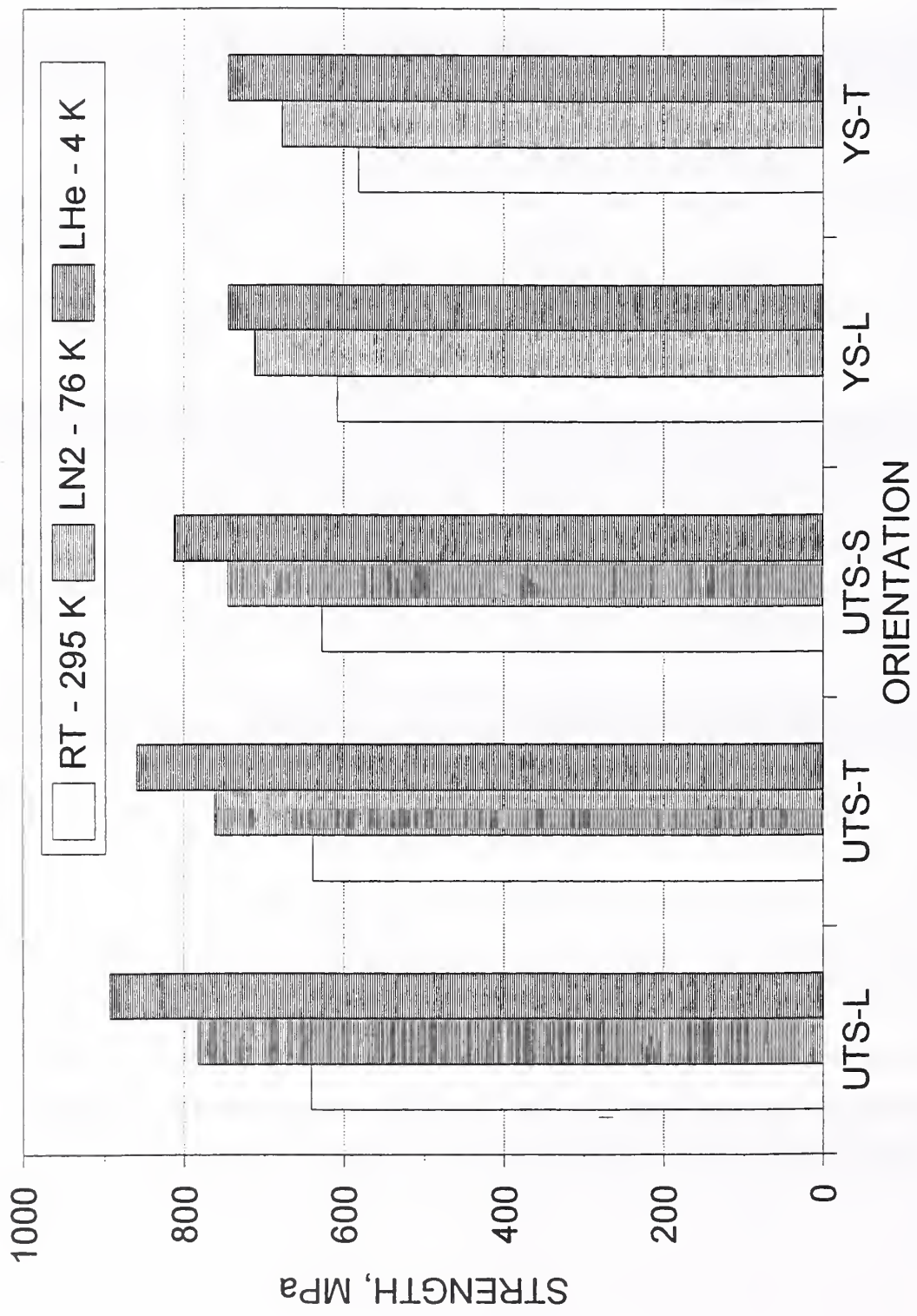
7

Fig. A2. Temperature dependence of the YS and UTS for Lot 1 as a function of orientation.
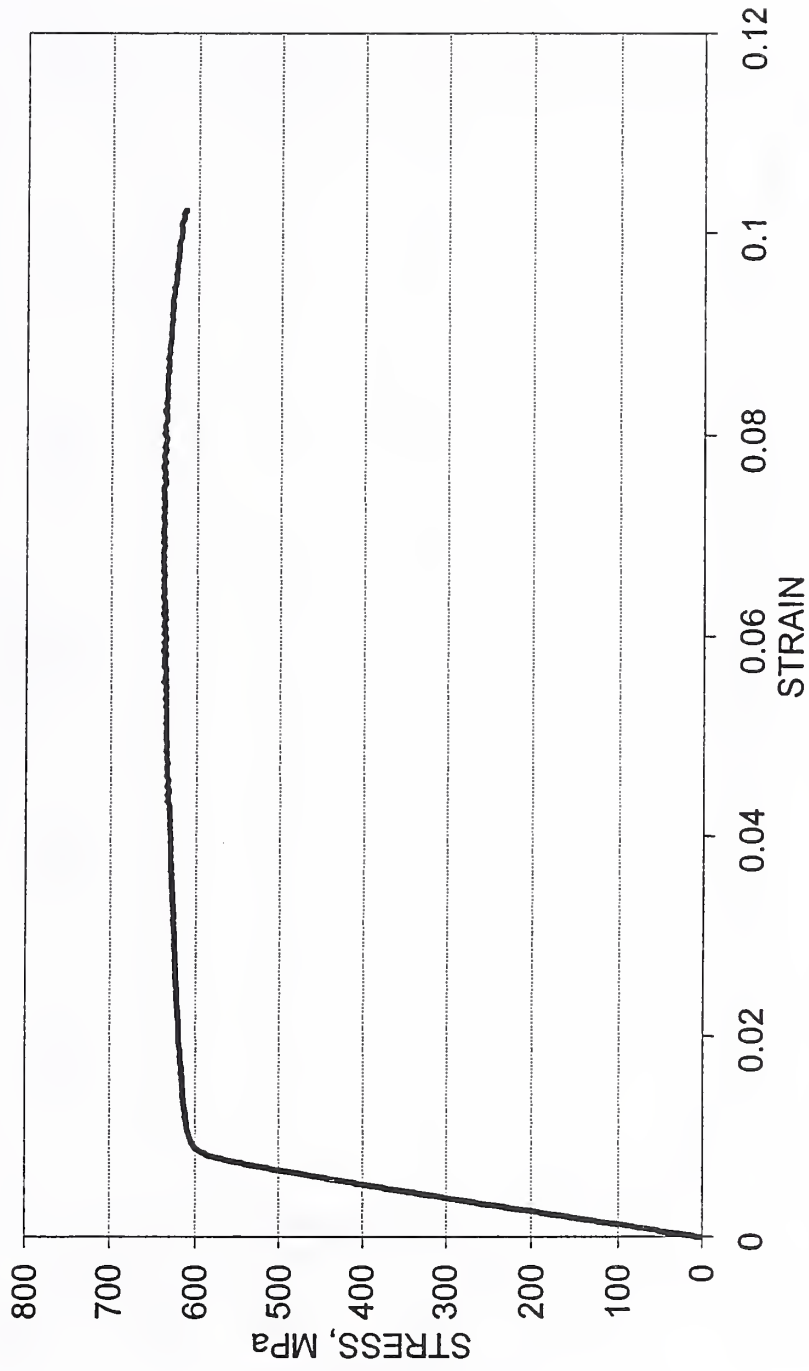
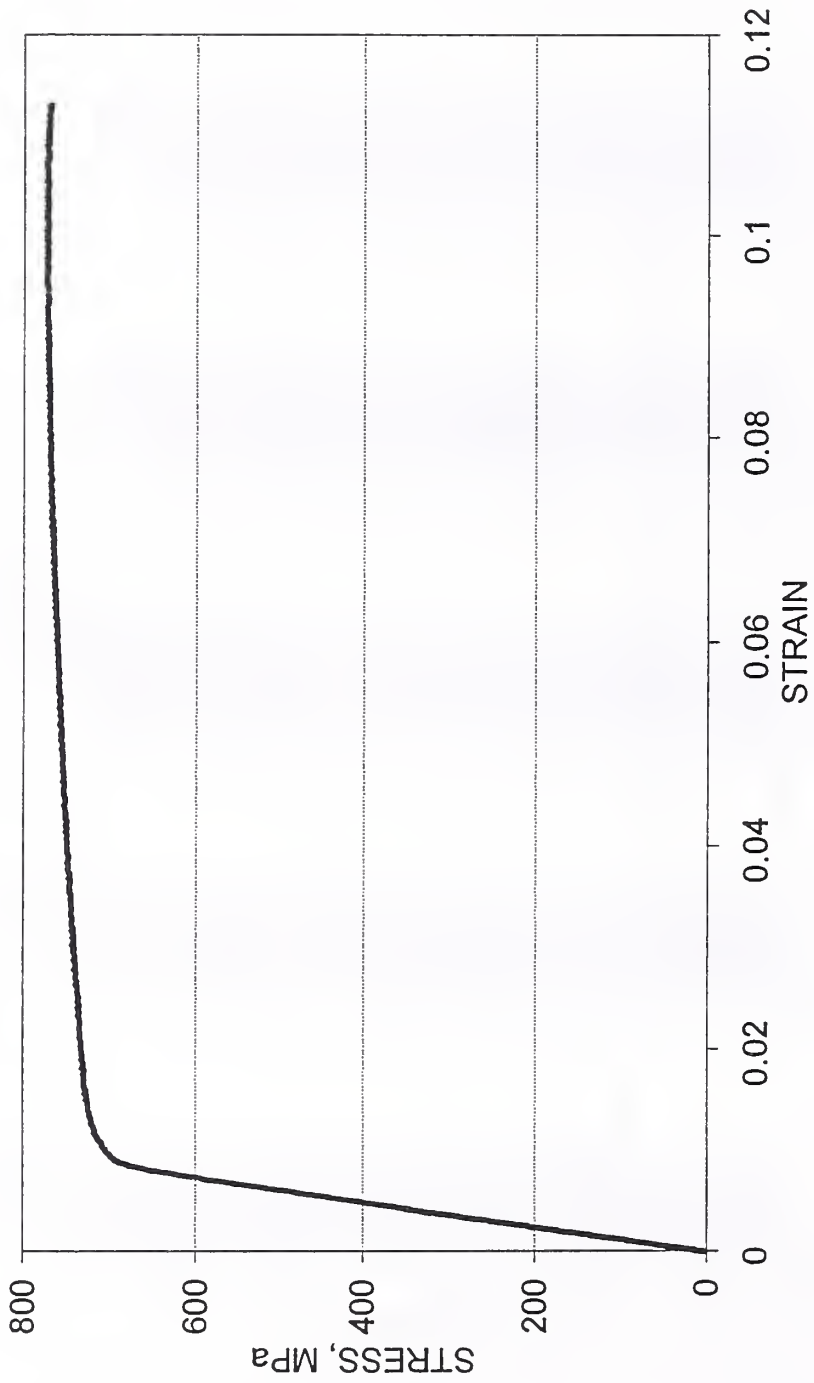Fig. A3 (a). Stress vs. strain for Lot 1, longitudinal specimen at RT.

LOT 1 - ALLOY 2094

@ LN2, SPEC. L3

Fig. A3 (b). Stress vs. strain for Lot 1, longitudinal specimen at LN2 temperature.
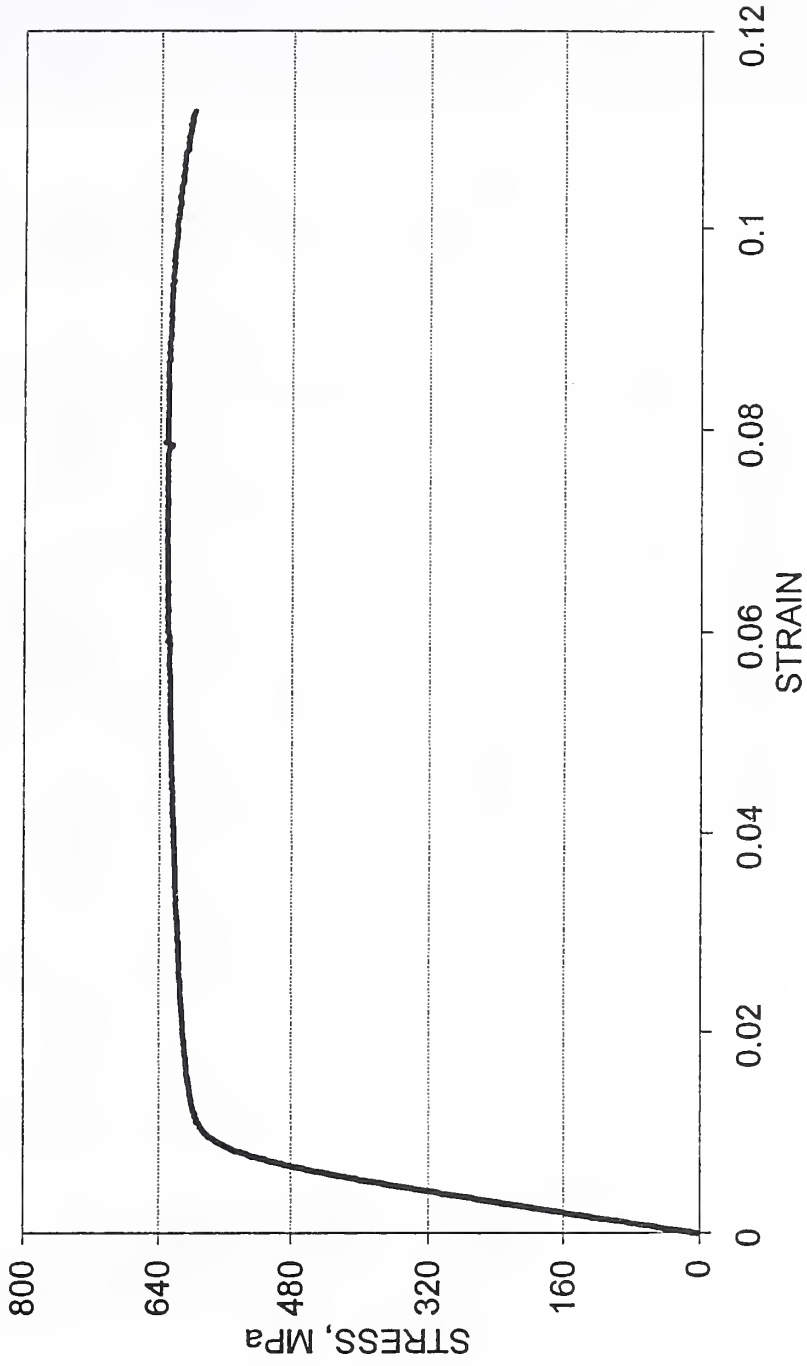
Fig. A4 (a). Stress vs. strain for Lot 1, long-transverse specimen at RT.
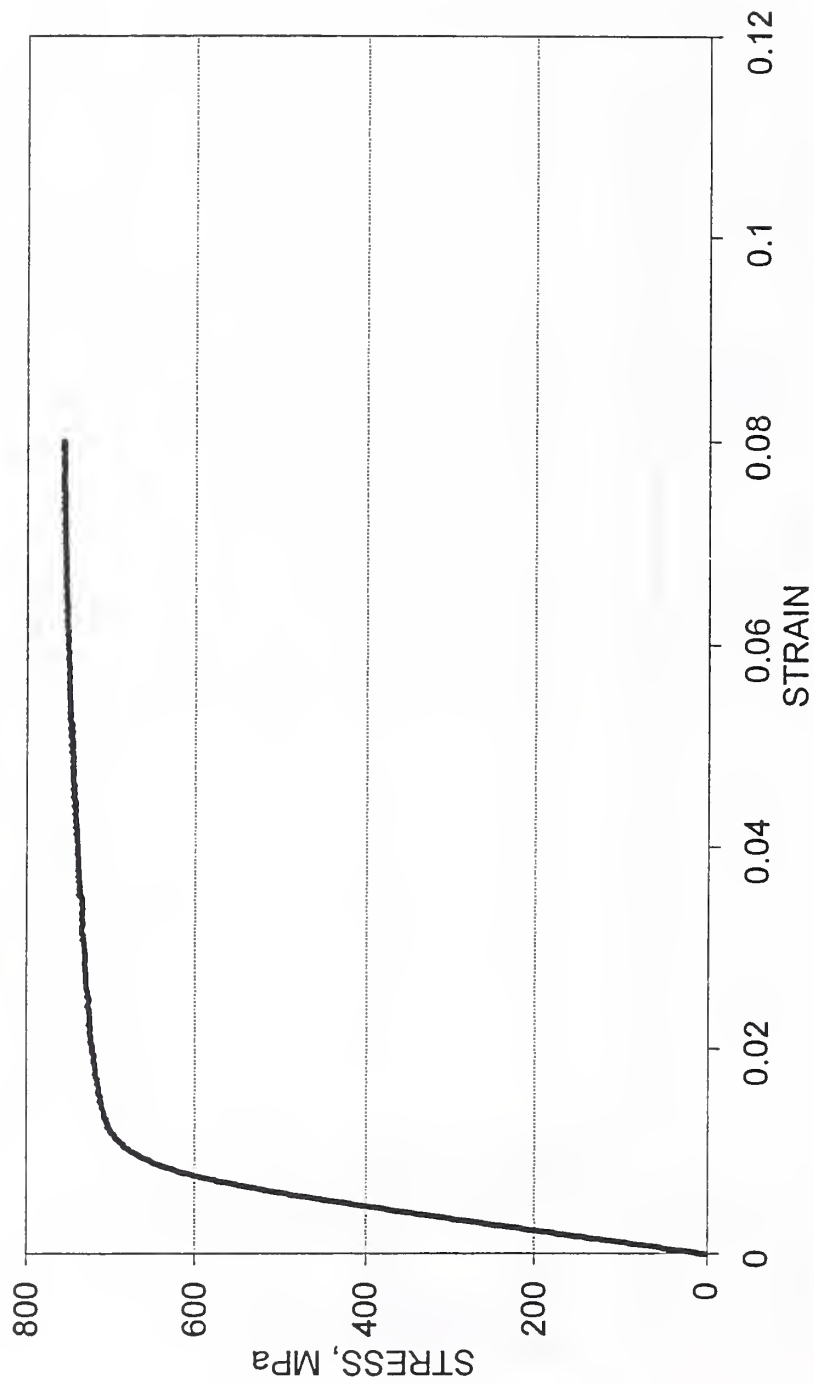
11

Fig. A4 (b). Stress vs. strain for Lot 1, long-transverse specimen at LN2 temperature.

12

Table A3. Summary of tensile fracture stresses.

Lot, orientation, temperature	Fracture stress, MPa	Stress concentration, a/R	Critical nucleation stress, MPa	σ_n/UTS
Lot 1, T, 295 K	769	0.50	1144	1.83
76 K	847	0.11	1171	1.57
4 K	937	0.11	1295	1.54
Lot 1, L, 295 K	764	0.10	1053	1.68
76 K	887	0.11	1225	1.60
4 K	1007	0.11	1391	1.59
Lot 1, S, 295 K	661	0.21	937	1.53
76 K	757	0.10	1043	1.42
4 K	824	0.10	1135	1.43
Lot 2, T, 295 K	778	0.49	1168	1.83
76 K	836	0.11	1156	1.55
4 K	943	0.11	1303	1.56
Lot 2, L, 295 K	772	0.49	1146	1.78
76 K	873	0.11	1207	1.57
4 K	974	0.11	1360	1.57
Lot 3, T, 295 K	712	0.49	1041	1.76
76 K	811	0.11	1120	1.54
4 K	918	0.11	1268	1.55
Lot 3, L, 295 K	754	0.20	1066	1.74
76 K	861	0.11	1189	1.57
4 K	997	0.10	1376	1.59
Lot 3, S, 295 K	713	0.16	1001	1.59
76 K	786	0.08	1077	1.44
4 K	794	0.08	1088	1.40

Table A4. Summary of fracture toughness test results (in MPa·m$^{1/2}$) with short-bar specimens, W/B = 2.0.

T., K	L-T	T-L	S-L
LOT 1			
295	20,21,21 (J)	24,25,24 (J)	19,18,20 (J)
76	42,42,43 (S-OP)	29,31,31 (S)	17,19,17 (J)
4	49,47 (J)	34,37,34 (S & J)	18,18,18 (J)
LOT 2			
295	32,30,32 (J-0P)	30,30,32 (J)	27,25,24 (J)
76	46,40,44 (S)	27,28,31 (S & J)	17,18,17 (J)
4	47,53,52 (J-OP)	31,39,30 (J)	16,16,17 (J)
LOT 3			
295	28,29,29 (J-OP)	27,33,30 (J)	29,24,29 (J)
76	40,38,34 (S-OP)	26,28,27 (S)	20,19,21 (J)
4	49,46,52 (J-OP)	34,35,29 (J)	19,20,18 (J)

S = smooth crack growth
J = crack jump behavior
OP = out of plane cracking after critical load

14

Figure A5 shows a plot of the temperature dependence of the toughness for each alloy. The toughness is always lowest for the S-L orientation. The toughness for the S-L orientation of each lot is plotted in **Fig. A6** vs. temperature. The S-L toughness of lots 2 and 3 decreases significantly with lower test temperature. For Lot 1, the S-L toughness is nearly independent of temperature.

Fractography:

The macroscopic appearance of the longitudinal tensile specimens was predominantly shear, a flat fracture oriented 45° to the tensile axis. Small delaminations were observed on the predominantly flat fracture surfaces of specimens oriented in the long-transverse direction with respect to the rolling direction. The short-transverse tensile specimens exhibited flat surfaces that were perpendicular to the tensile axis. For the three tensile orientations (longitudinal, long-transverse, and short-transverse), temperature had little effect on the fracture appearance.

At higher magnification, the features on the fracture surfaces of the longitudinal and long-transverse tensile specimens are similar. **Figure A7** shows the appearance of a longitudinal specimens fractured in LHe. There are intergranular facets and little evidence of void nucleation from the constituent particles.

For the short-transverse tensile specimens, representative fractographs are shown in **Fig. A8**. The RT specimens exhibit a mixed fracture appearance; intergranular features are interspersed with shallow dimples from second-phase particles as big as 10 µm in diameter. Below RT, the fractures are predominantly intergranular.

The fracture surface appearance of the toughness specimens from the L-T orientation was a function of test temperature. **Figure A9 (a)** shows the features of a RT fracture surface in the L-T orientation. No delaminations were observed on the macroscopic level and numerous fine dimples that nucleate from constituent particles are found at higher magnification. In **Fig. A9 (b)**, the features of a cryogenic L-T fracture surface are seen. Numerous delaminations of various sizes are observed macroscopically, but the fine features are very similar to those found at RT in **Fig. A9 (a)**.

For short-bar specimens oriented in the T-L and S-L direction, there were very few delaminations and little difference in macroscopic fracture appearance due to temperature. The fine features on the T-L fracture surfaces are similar to those observed at high magnification for the L-T specimens in **Fig. A9**. However, the fine features on S-L fracture surfaces do change with testing temperature. **Figure A10** shows similar areas from S-L specimens tested at RT and in LN2. The one tested at RT (**Fig. A10 (a)**) has a mixed appearance with intergranular features and dimpled rupture from particles as large as 10 µm in diameter. In the LN2 environment, the fracture surface (**Fig. A10 (b)**) is intergranular with no evidence of cracked constituent particles.
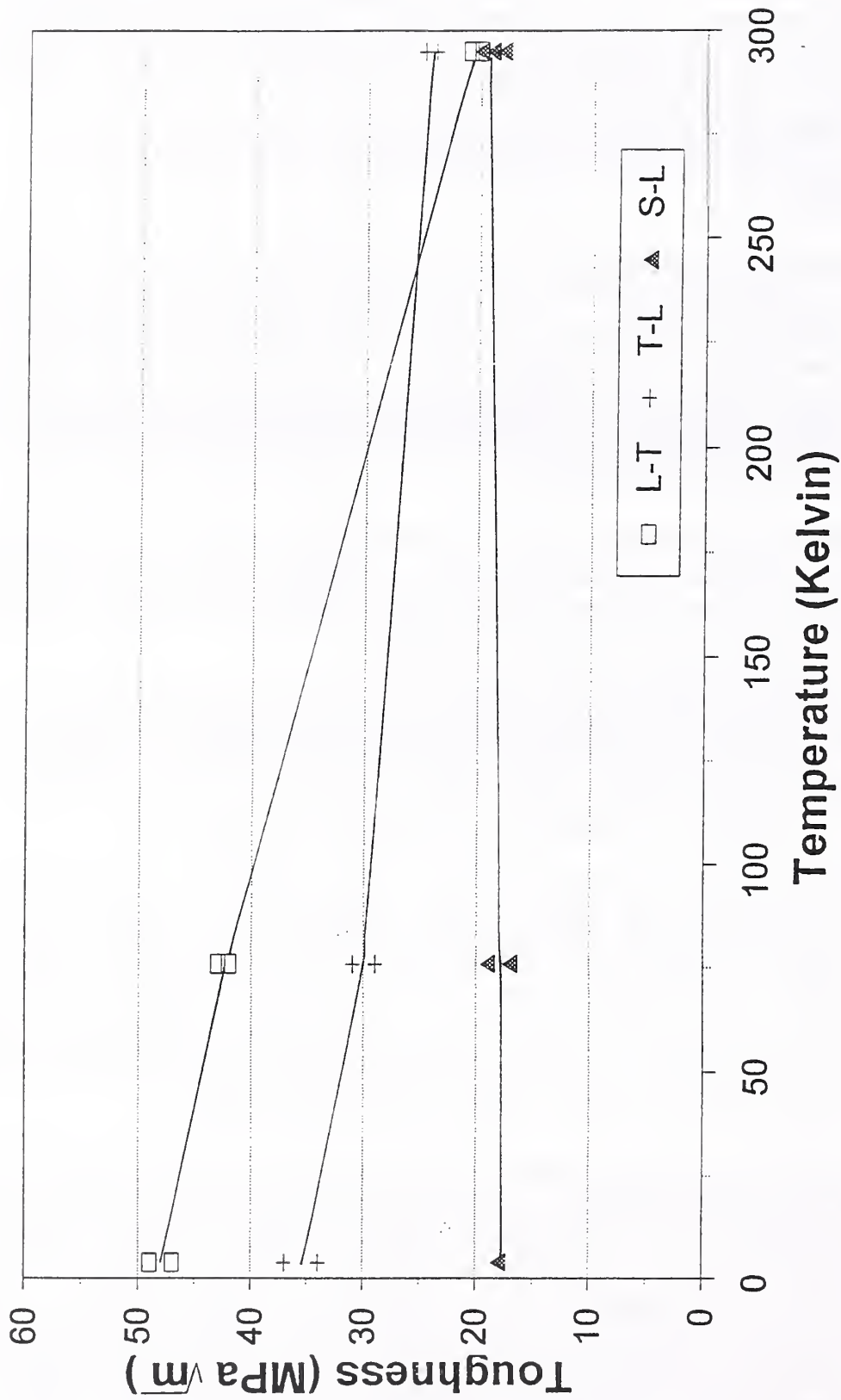
15

LOT 1

Temperature (Kelvin)

Toughness (MPa √ m̄)

□ L-T   + T-L   ▲ S-L

Fig.   A5   (a).   Fracture   toughness   of   Lot   1   specimens   plotted   vs.   temperature.
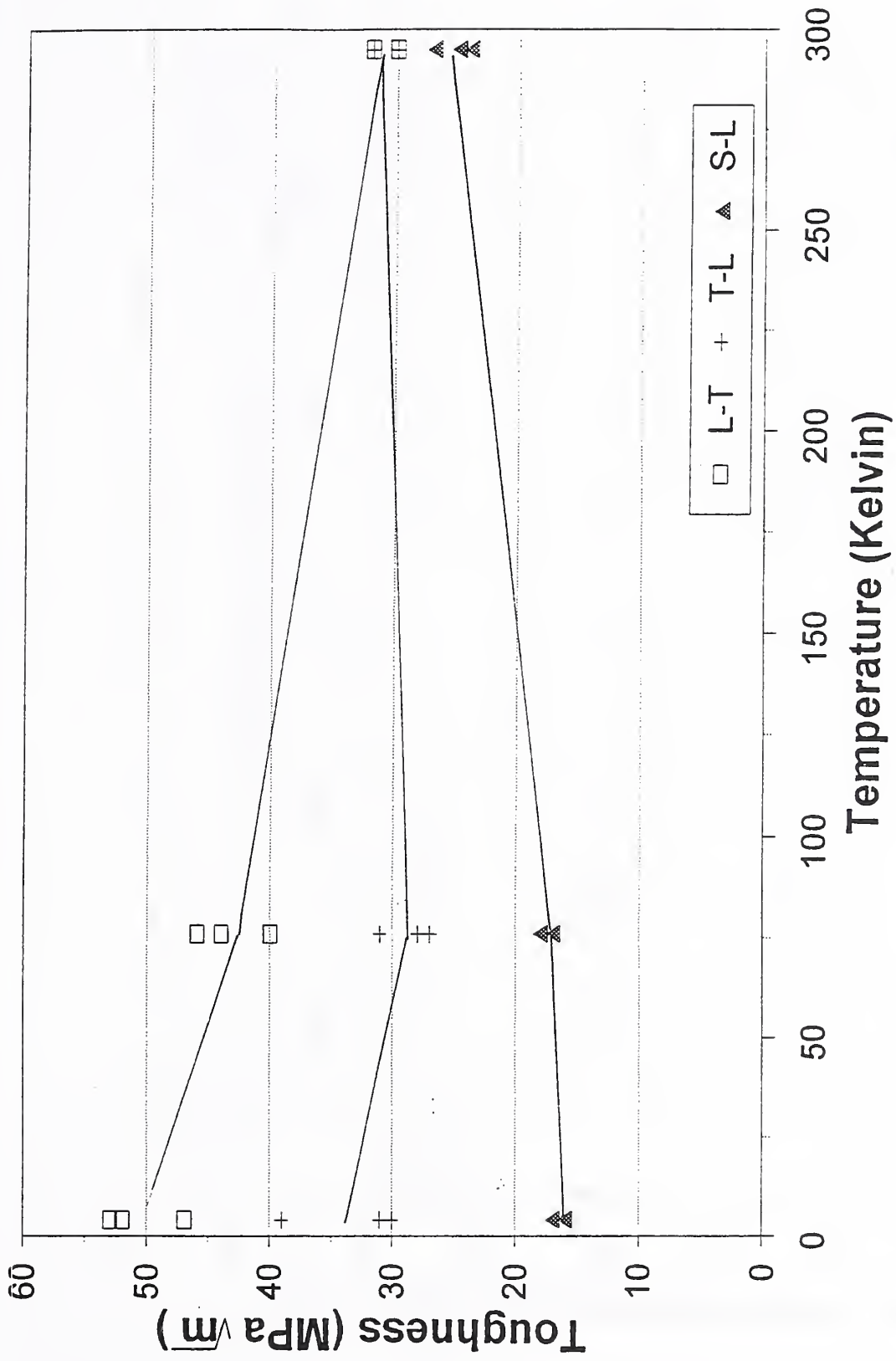
16

Fig. A5 (b). Fracture toughness of Lot 2 specimens plotted vs. temperature.
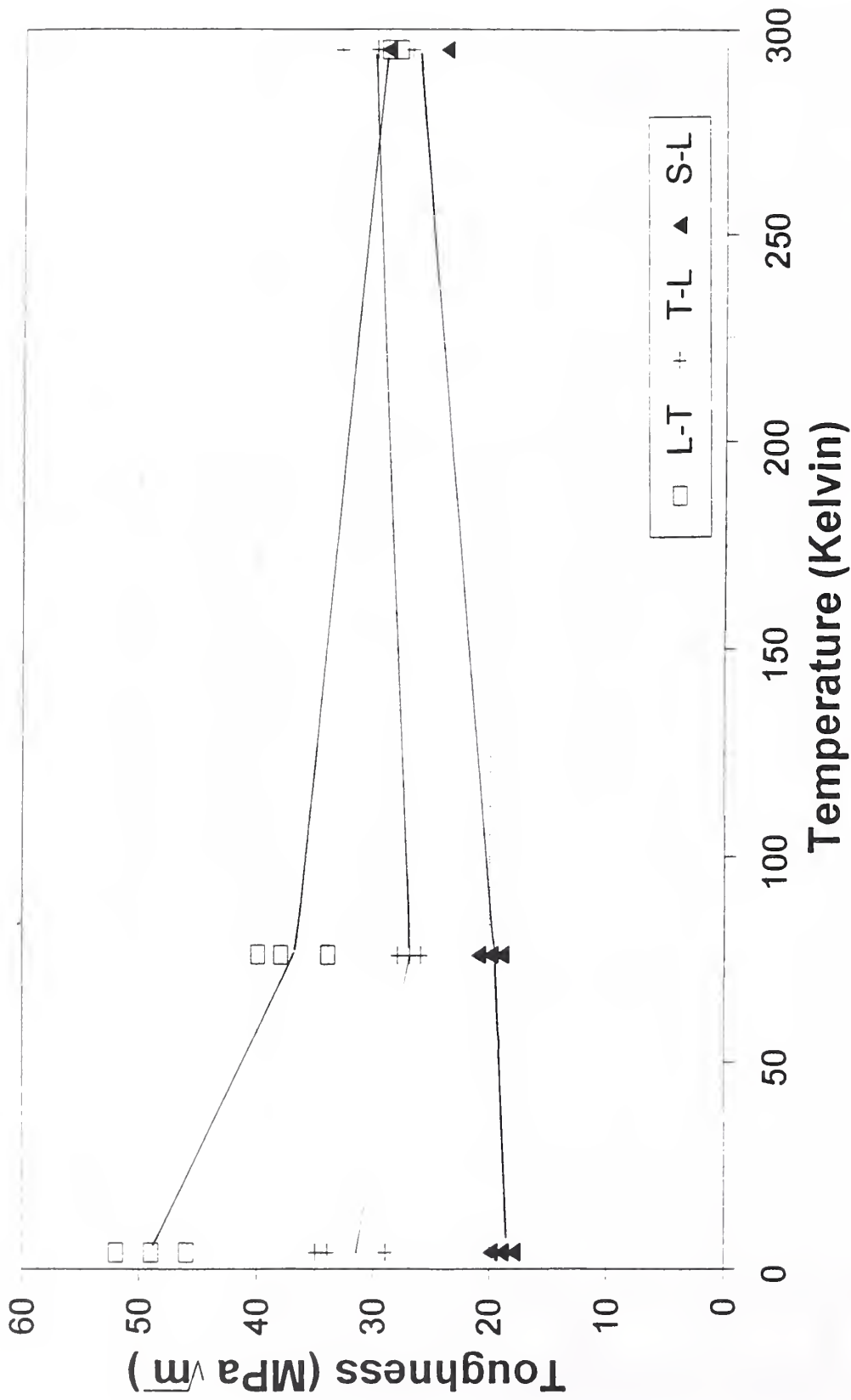
17

Fig. A5 (c). Fracture toughness of Lot 3 specimens plotted vs. temperature.
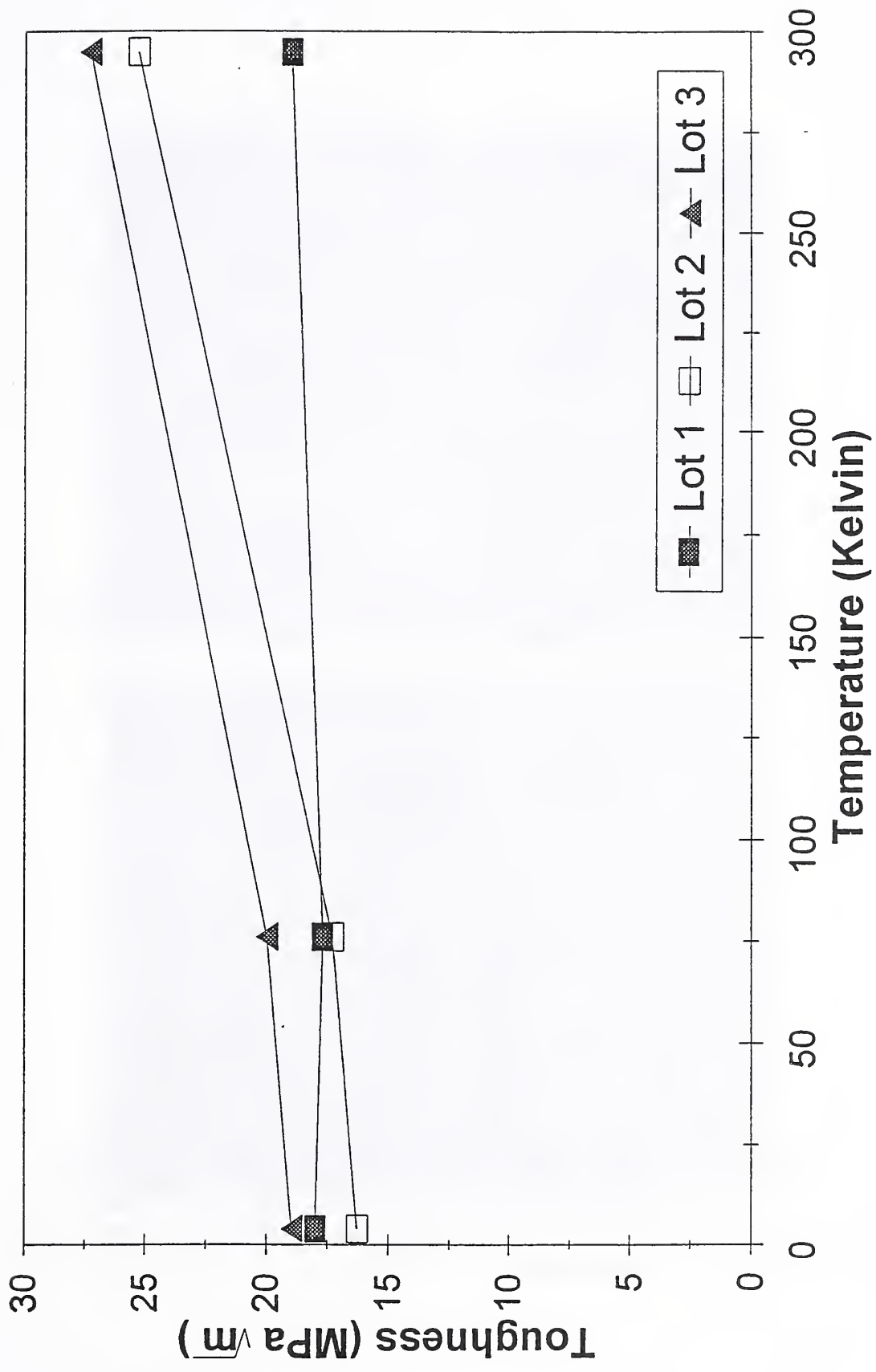
Fig. A6.   Average toughness in S-L orientation plotted vs. temperature.
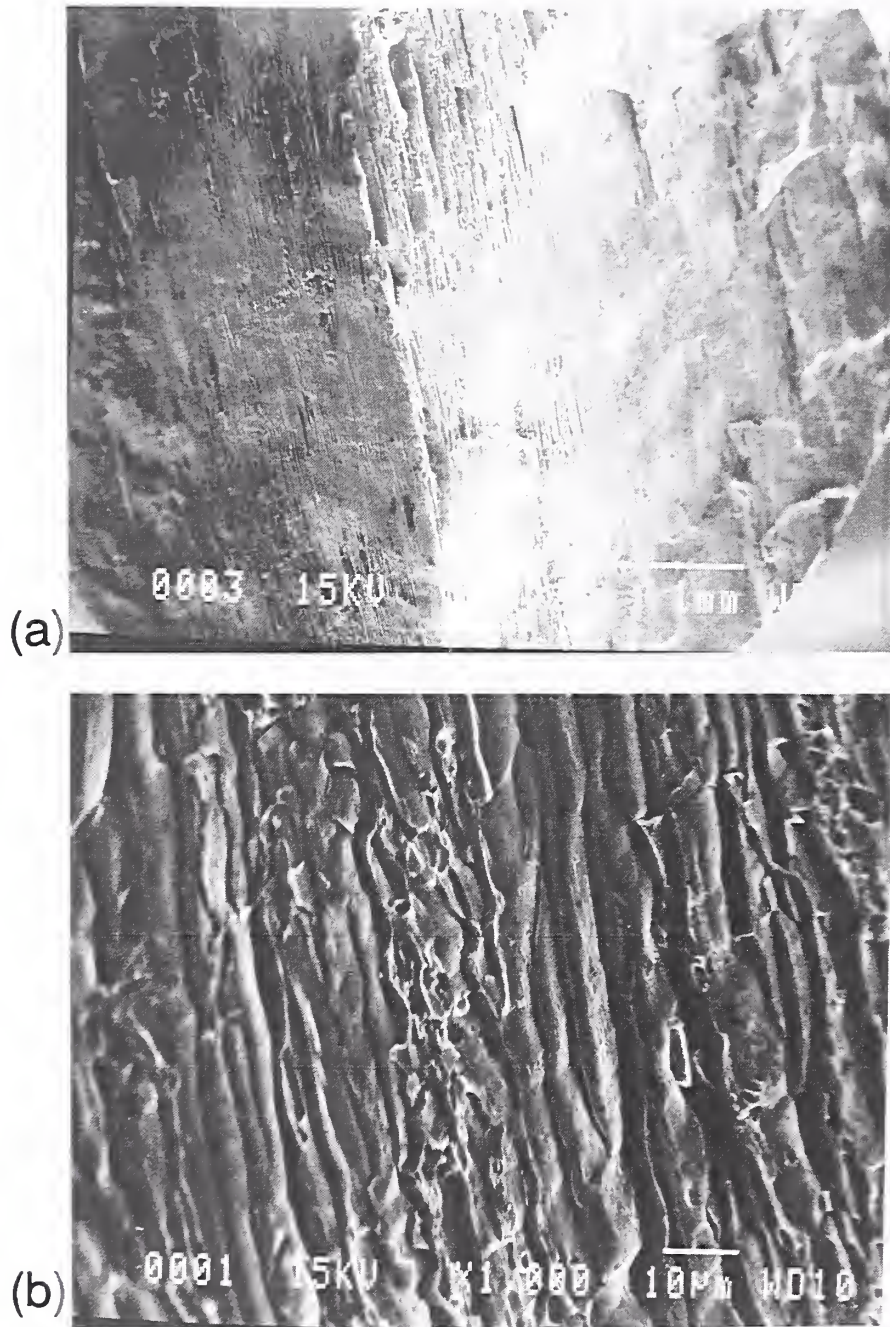
Fig. A7.   SEM fractograph showing the longitudinal tensile specimen from Lot
             1, LHe test temperature.
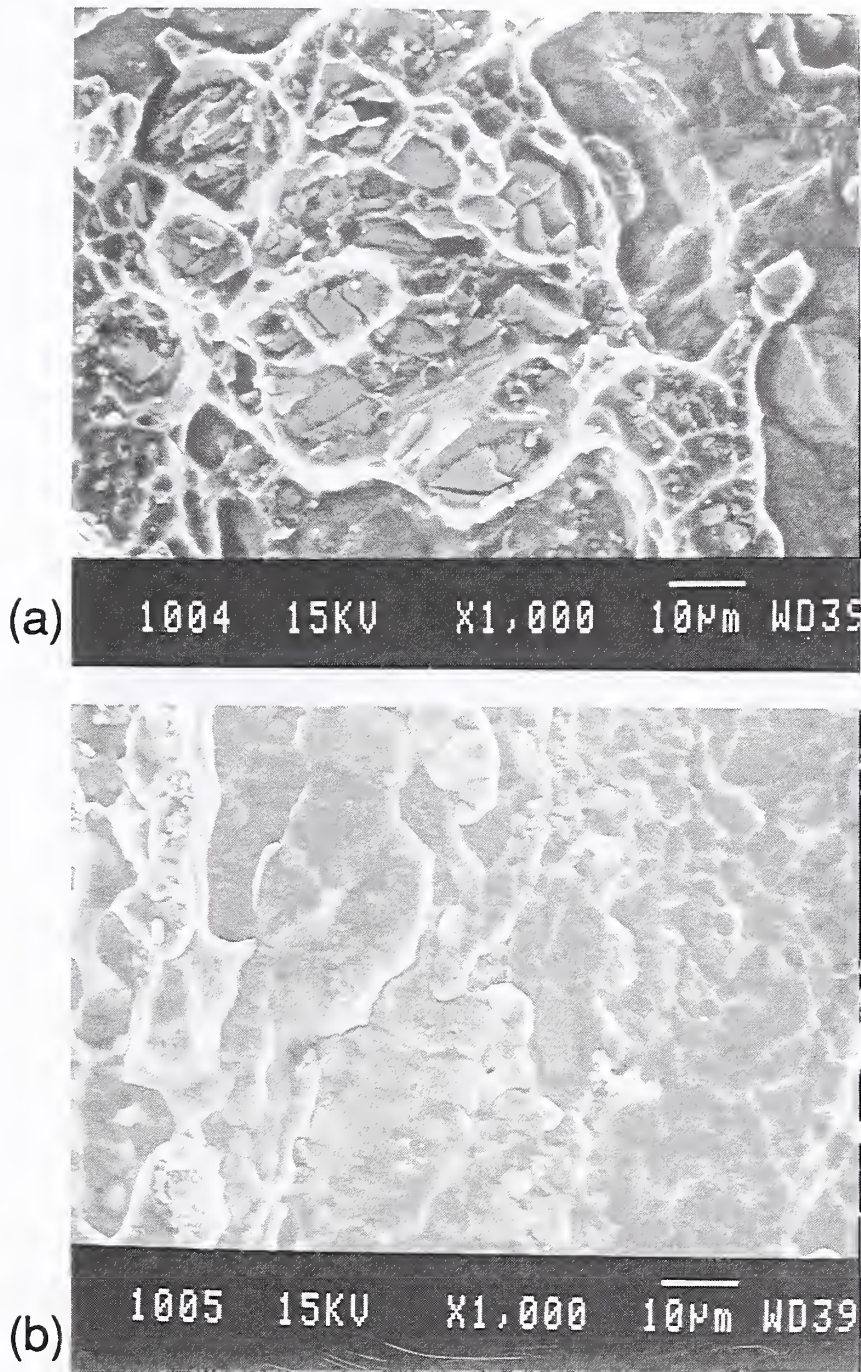
Fig. A8.   SEM fractograph showing the short-transverse tensile specimen from
Lot 3, (a) RT test and (b) LN2 test temperature.

(a) 1001 15KV X50 100μm WD39

(b) 1005 15KV X20 1mm WD37

Fig. A9.   SEM fractograph showing the L-T fracture toughness specimen from
            Lot 3, (a) RT test and (b) LN2 test temperature.

(a)

    1017   15KV   X1,000   10μm WD39

(b)

    1020   15KV   X1,000   10μm WD39
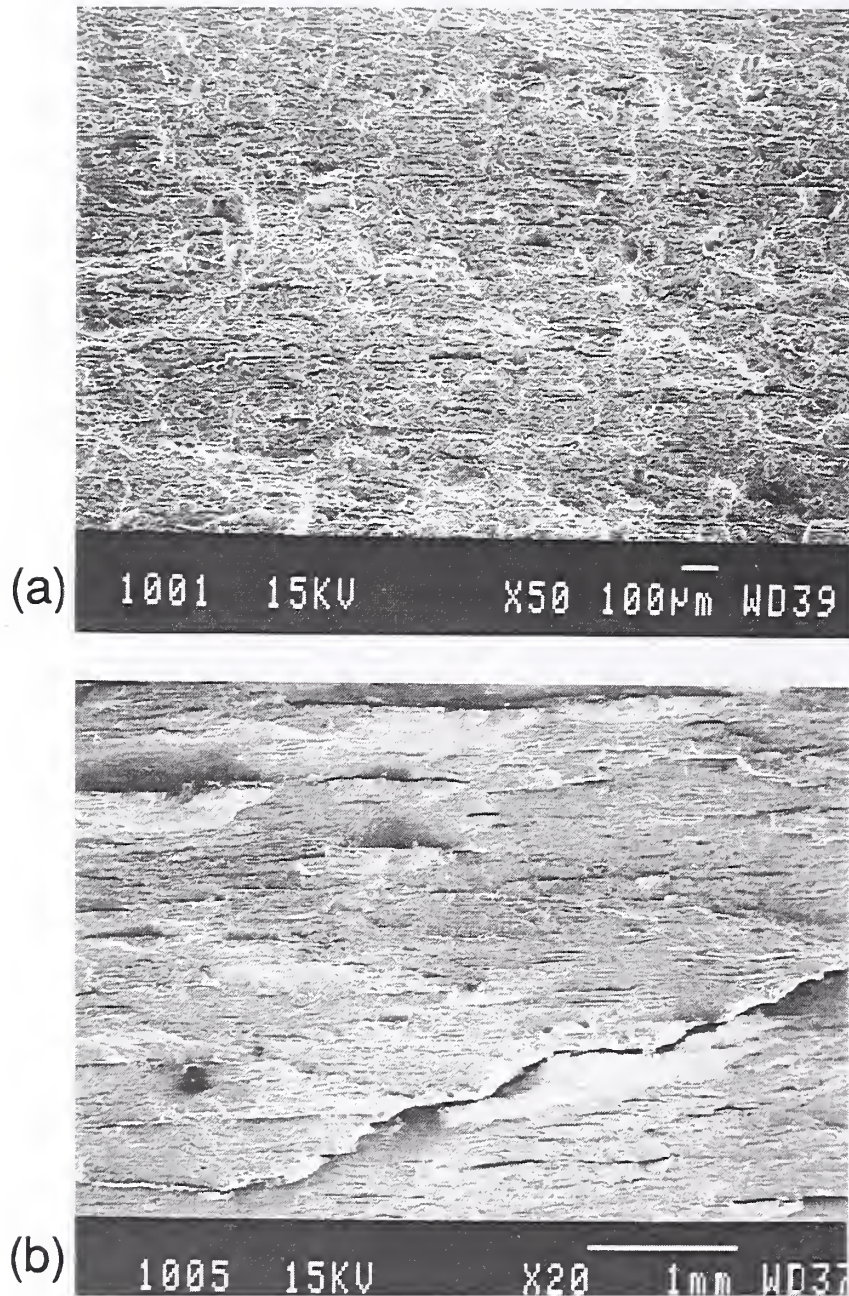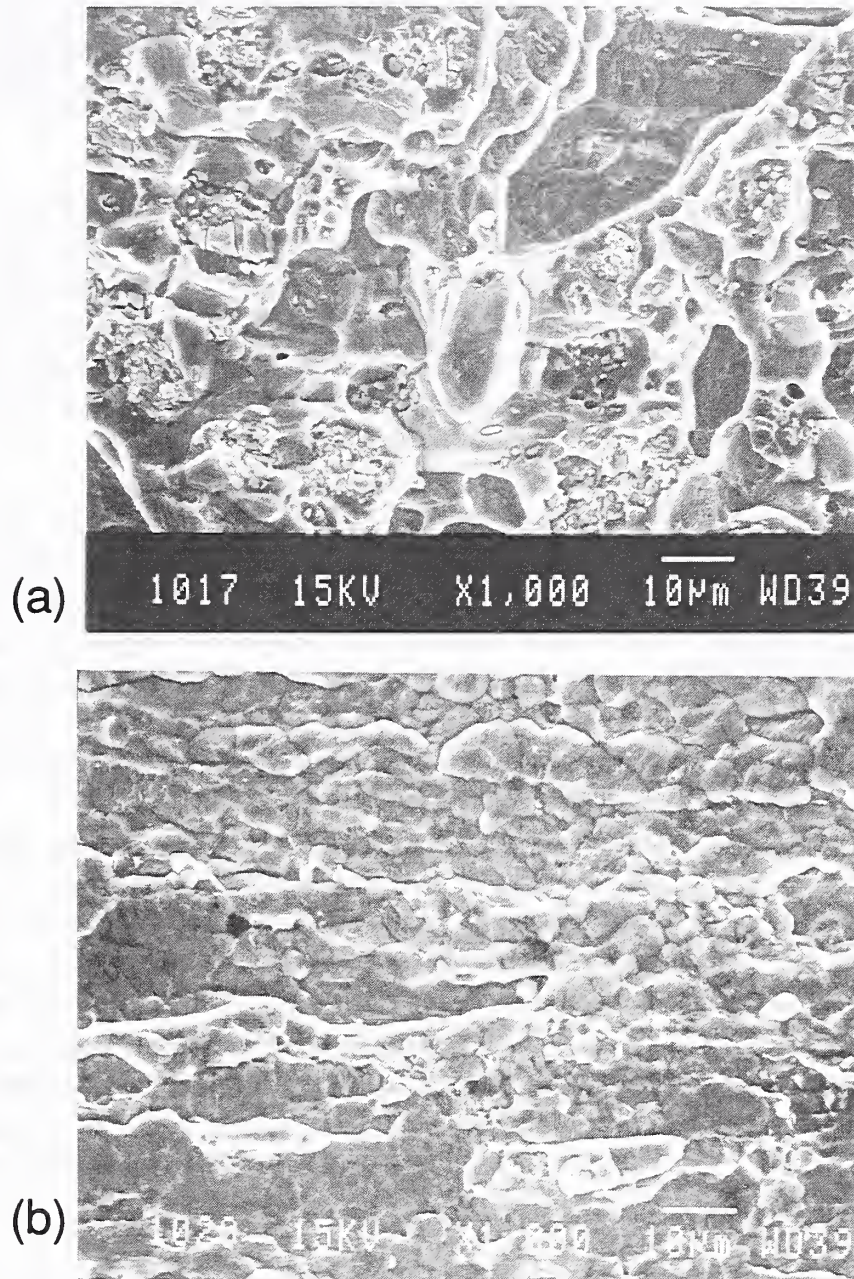
Fig. A10.   SEM fractograph showing the S-L fracture toughness specimen from
             Lot 3, (a) RT test and (b) LN2 test temperature.

23

DISCUSSION

Overall, the results show that there are only slight differences among the mechanical properties of the three alloys from RT down to LHe temperature. Lot 3 with less Li does have slightly lower YS and UTS than the other two lots, but the difference is less than 10%. Given the relative insensitivity of tensile properties to composition, other factors like weldability or density can be optimized.

Besides the absolute value of the mechanical properties, another important consideration is the temperature dependence of the properties. The ratios for YS and toughness are shown in **Fig. A11**. All three lots show ratios for the YS and $K_{Iv} > 1$ for the L-T orientation. Only Lot 1 has the desired ratios in the T-L orientation as well, and that is because its RT toughness is lower than for the other two lots. In LN2 and LHe, the toughnesses are nearly identical. No composition exhibits a desirable toughness ratio in the S-L orientation.

The mechanism that produces the higher ratios of CT to RT toughness in the L-T orientation is the source of some debate. Glazer et al. [A16] looked at Alloy 2090 at various temperatures and decided that the increase in toughness at CT was due to an increased strain hardening at CT. Rao and Ritchie [A17] came to a different conclusion in their work on Alloy 2090. They attributed the increase in toughness at low temperature to the formation of delaminations at the crack tip. The delaminations relax the plane strain conditions, leading to plane stress fracture conditions and higher toughness.

In this study of the Al-Cu-Li-Mg-Ag-Zr system, the tensile properties are similar for the long-transverse and longitudinal orientations and there is a slight increase in uniform strain as the test temperature goes down. For all three lots, the uniform strain increases in both the T and the L tensile orientations when the temperature decreases from RT to LN2. If toughness were higher at CT than at RT in the L-T orientation because of increased strain hardening, we would expect to see a similar increased toughness in the T-L orientation. There are no consistent data to support the conclusions of Glazer et al. [A16]. On the other hand, delaminations appear on the fracture surfaces of specimens tested below RT, but rarely are delaminations observed on RT fracture surfaces. The fractographic evidence supports the conclusions of Rao and Ritchie [A17].

The correlation between tensile properties and fracture toughness in high-strength alloys has been of fundamental interest for many years [A18,A19]. If there is a similar fracture mechanism in both uniaxial tension and plane-strain fracture testing, then there could be a correlation between the two which could predict the results of subsequent testing. In our study, the fracture mechanisms in uniaxial tension and toughness testing are usually not the same (see results section on fractography). However, for Lot 3 in the short-transverse direction, the fracture surface from the tensile specimen is quite similar to the short-bar specimen in the S-L orientation (see **Figs. A8 and A10**).
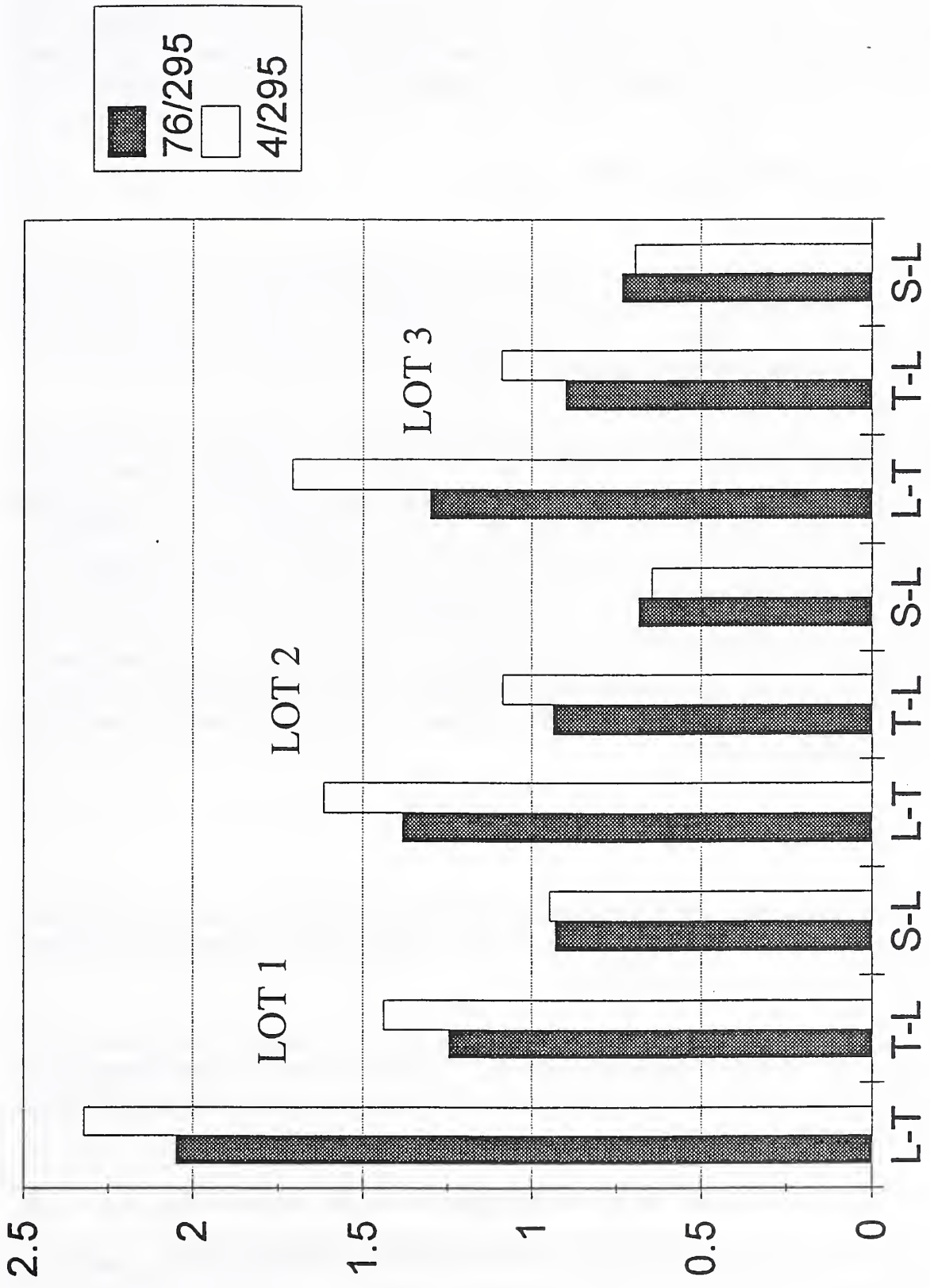
Fig. A11.   Ratio of fracture toughness at CT to RT for each Lot.

To examine the correlation between fracture in uniaxial tension and fracture toughness, we assume that the stresses in the short-bar and tensile specimens are comparable and that the fracture toughness is controlled by a critical stress. Given these assumptions, we can use the model for stress-controlled fracture described previously [15]:

$$K_{Ic} \approx \{[\sigma^*]^{(1+n)/2n} / [\sigma_y]^{(1-n)/2n}\} \cdot \{L_0\}^{1/2}, \qquad (A3)$$

where σ^* is the local fracture stress, n is the strain-hardening exponent, and σ_y is the YS. The term L_0 is a characteristic distance that is related to the microstructure and does not change with test temperature. If these assumptions are valid, then toughness is proportional to the ratio of the critical interfacial stress in tension to the UTS.

The average fracture toughness is plotted against the ratio of critical interfacial stress to UTS in **Fig A12** for Lot 3 specimens in the S-L and L-T orientation. In the S-L and short-transverse orientations, both values decrease with temperature. In the longitudinal and L-T orientations, the increase in toughness at lower temperature is not reflected by an increase in the ratio of critical fracture stress to UTS. This evidence supports the earlier point made in the discussion regarding the increase in toughness with decreasing temperature. If the intrinsic toughness of the material is improving at low temperature, then the ratio of critical fracture stress to UTS will also improve. The increase in toughness at CT for the L-T orientation for alloys 2094 and 2095 appears to be due to extrinsic factors from delaminations on the fracture surface and/or crack tip branching, rather than instrinsic reasons.

CONCLUSIONS

1.   There is less than 10% difference between the tensile flow stresses of the three alloys from the Al-Cu-Li-Mg-Ag-Zr system. The tensile flow and fracture stresses all increase at lower temperature.

2.   For all three alloys, toughness in L-T orientation was the highest and demonstrates increasing values with lower temperature. The effect is due to extrinsic toughening mechanisms such as delaminations and crack branching rather than any change in the deformation behavior.

3.   All three alloys exhibit the lowest toughness in the S-L orientation.

4.   Overall, there appears to be little difference in cryogenic mechanical properties of the three alloys in the Al-Cu-Li-Mg-Ag-Zr system.
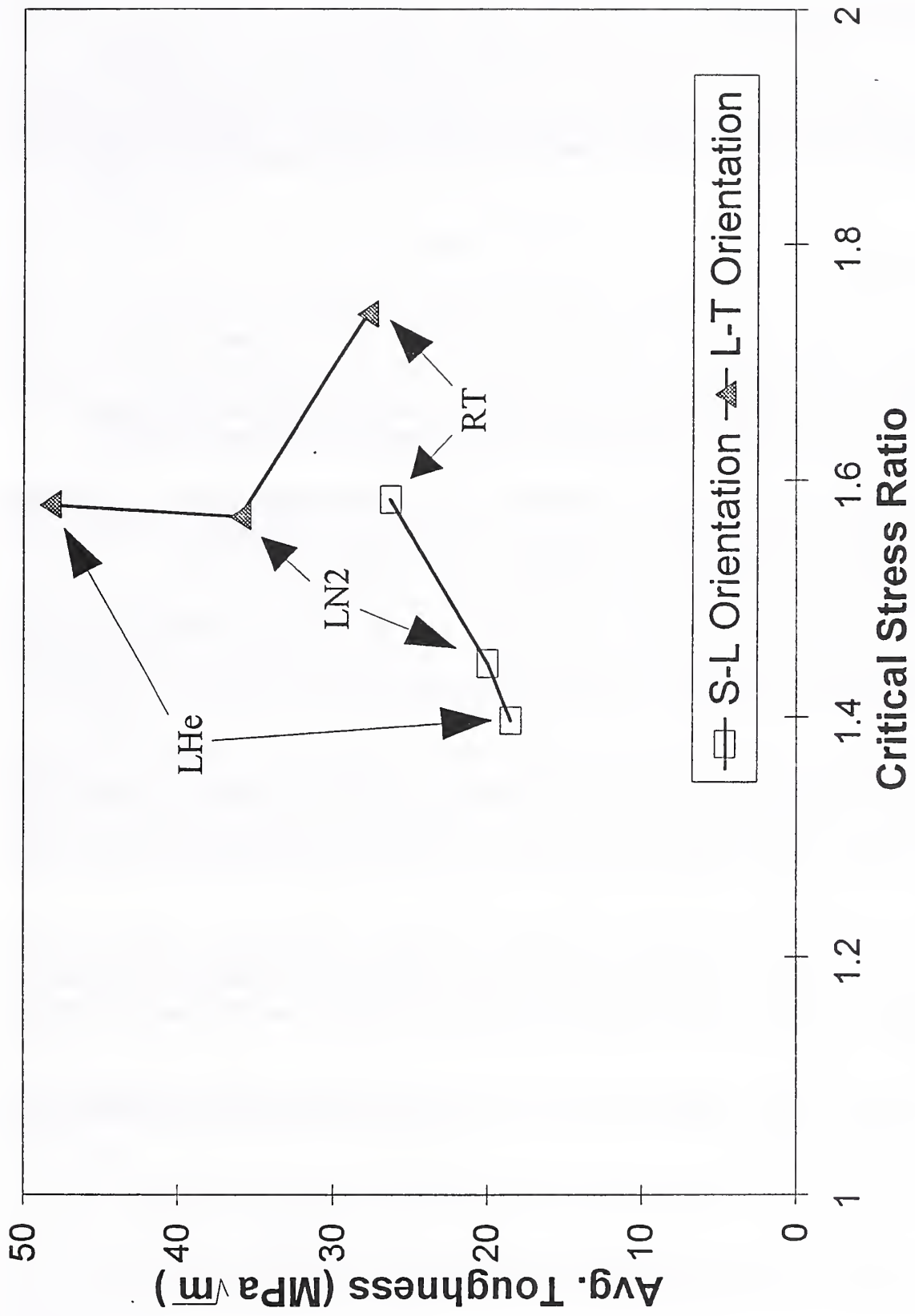
Fig. A12.   Plot of average toughness vs. the critical stress ratio (σ_c/UTS) in the tensile test as a function of test temperature for Lot 1. Specimens were taken either through the thickness of the plate (S-L) or against the rolling direction, but in the plane of the plate (L-T).

27

REFERENCES

A1. T.H. Sanders and E.S. Balmuth, Metal Progress, Vol. 113, March 1978, pp. 32-37.

A2. W.T. Tack and L.W. Loechel, in Aluminum-Lithium Vol.2, eds. M. Peters and P.-J. Winkler, Informationsgesellschaft, Verlag, Germany, 1992, pp. 415-420.

A3. L.S. Kramer, F.H. Heubaum, and J.R. Pickens, in Aluminum-Lithium Alloys, Vol. III, eds. T.H. Sanders Jr. and E.A. Starke Jr., Materials and Component Engineering Publications, Birmingham, U.K., 1989, pp. 1415-1424.

A4. J.R. Pickens, F.H. Heubaum, T.J. Langan, and L.S. Kramer, in Aluminum-Lithium Alloys, Vol. III, eds. T.H. Sanders Jr. and E.A. Starke Jr., Materials and Component Engineering Publications, Birmingham, U.K., 1989, pp. 1397-1414.

A5. R.P. Reed, P.T. Purtscher, N.J. Simon, J.D. McColskey, R.P. Walsh, J.R. Berger, E.S. Drexler, and R.L. Santoyo, "Aluminum Alloys for ALS Cryogenic Tanks: Comparative Measurements of Cryogenic Mechanical Properties of Al-Li Alloys and Alloy 2219," Air Force Report No. PL-TR-91-3073, Edwards Air Force Base, CA, Oct. 1991.

A6. P.T. Purtscher, M. Austin, S. Kim, and D. Rule, "Aluminum-Lithium Alloys: Surface-Cracked Tension Fracture Tests and Physical and Thermal Properties at Cryogenic Temperatures," National Institute of Standards and Technology, NISTIR 3986, 1992.

A7. ASTM E 8-89b, American Society for Testing and Materials, Philadelphia PA, 1990, pp. 130-160.

A8. P.T. Purtscher, Scripta Metall. et Mater., Vol. 26, 1992, pp. 343-346.

A9. G. Krauss, in Harterei-Technische Mitteilungen, Vol. 46, 1991, pp. 7-15.

A10. J.A. Sanders, et al., in <u>Fundamentals of Aging and Tempering in Bainitic Steel Products</u>, Iron and Steel Society, Warrendale, PA, 1992, pp.67-76.

A11. P.T. Purtscher and Y.W. Cheng, in <u>34th Mechanical Working and Steel Processing Conference Proceedings</u>, Iron and Steel Society, Warrendale, PA, 1993, pp. 331-340.

A12. A.S. Argon, J. Im, and R. Safoglu, Metall. Trans., Vol. 6A, 1975, pp. 825-838.

A13. A.S. Argon, J. Im, and A. Needleman, Metall. Trans., Vol. 6A, 1975, pp. 815-824.

A14. P.T. Purtscher, J.D. McColsky, and E.S. Drexler, in <u>Chevron-Notch Fracture Test Experience</u>, STP 1172, eds. K.R. Brown and F.I. Baratta, American Society for Testing and Materials, Philadelphia PA, 1992, pp. 110-130.

A15. ASTM E 399-83, American Society for Testing and Materials, Philadelphia PA, 1990, pp. 488-512.

A16. J. Glazer, S.L. Verzasconi, R.R. Sawtell, and J.W. Morris, Jr., Metall. Trans., Vol. 18A, 1987, pp. 1695-1701.

A17. K.T.V. Rao and R.O. Ritchie, Acta Metall. Mater., Vol 38, No. 11, 1990, pp. 2309-2326.

A18. K.-H. Schwalbe, Eng. Fract. Mech., Vol. 6, 1974, pp. 415-431.

A19. K.-H. Schwalbe, Eng. Fract. Mech., Vol. 9, 1977, pp. 795-832.

PART B

SURFACE FLAW FRACTURE TESTING OF ALLOY 2090 IN DIFFERENT PRODUCT FORMS AT ROOM AND CRYOGENIC TEMPERATURES
P.T. Purtscher

INTRODUCTION

This work is a continuation of the program for surface-cracked tension fracture testing of Al-Li alloys [1]. In the past, the program looked at the properties of Al-Li alloys in the form of wrought plates with two thicknesses, 12.7 and 19.1 mm. If Al-Li alloys are to be used in aerospace structures like the fuel tank on the Space Shuttle, many product forms in addition to plates will be used and need to be characterized.

We have studied the fracture behavior of Alloy 2090 in three different product forms: extrusions, wrought sheets (less than 6.4 mm thick), and welds. The goal of the program is to measure the residual strength and defect tolerance of Al-Li alloys as a function of test temperature, and to characterize those features that promote an increased defect tolerance at cryogenic temperatures compared to room temperature. In the case of the plates which were tested previously [1], we found an increase in residual strength and toughness as the test temperature decreased from room temperature (RT) to cryogenic temperatures (CT). We attributed the increase in defect tolerance at lower temperature to the formation of delaminations on the fracture surface.

MATERIALS AND PROCEDURES

Three groups of specimens are used in this program: Alloy 2090 extrusions of ribbed panels with an L-shaped stiffener made in Russia; Alloy 2090-T83 sheet (two different sheets, lot # 212956, 5.92 mm thick and lot # 347281, 6.38 mm thick); and welds made from the Russian 2090 extrusions with type 2319 welding wire. The chemical compositions of the different 2090 alloys are shown in **Table B1**.

Table B1.   Chemical compositions of the 2090 alloys used in this study.

Product form	Cu	Li	Zr	Mg	Ti	Si	Fe	Zn
Extrusion[*]	2.68	2.22	0.13	0.01	0.03	0.05	0.09	0.02
Sheet-- lot 1	2.76	2.30	0.13	0.01	0.03	0.05	0.07	0.04
lot 2	2.56	2.13	0.12	0.01	0.02	0.05	0.06	0.05

[*] Composition from center of billet prior to extrusion.

The extrusions were made from solid ingots (360 mm x 700 mm cross section) by broach forging into hollow billets (418 x 306 x 640 mm). The forging temperature in the initial stage was 420°C and at the final stage, the temperature was 380°C. The extrusion was done at a billet and container temperature of 400°C. The extrusion rate was 0.6 m/min. The final thickness was 4.6 mm. After extrusion, the part was cut, unfolded, and straightened. The planar dimensions of the panel were 0.825 m wide and 3.02 m long. The panel was solution treated at 545°C for 45 min, water cooled, stretched 6%, and aged at 163°C for 1 day.

The welds were made with the variable polarity plasma arc (VPPA) process with the abutting edges dry machined, and the front and back surfaces of the panels manually wire-brushed.

Setup tests were run on the first sheet of 2090-T83 at room temperature in order to determine the approximate precracking conditions. There was insufficient material available from the first sheet for both room and cryogenic temperature testing. Duplicate tests were then run on dog-bone type specimens [1] (types A and B) from each of the three remaining groups according to the test matrix shown in **Table B2**. Type A specimens were larger (gage section is 200 mm long and 100 mm wide) than those from type B (gage section is 125 mm long and 63 mm wide). In the welded specimens, the crack was oriented along the weld so that the crack plane contained only weld metal.

31

Table B2.   Summary of test matrix for surface-cracked tension fracture
tests, type A and B.

Product form	Testing conditions		
	Ambient	LN2	LHe
Extrusions	4	4	4
Sheet	4	4	4
Welds	4	--	4

Fatigue precracking was performed at room temperature (approximately 295 K) and was usually done in tension-tension and with an R (minimum load divided by the maximum load) = 0.1. A few specimens were loaded for the initial precracking in three-point bending. The stress intensity factor at the maximum depth of the fatigue crack for the final increment of fatigue growth was typically 5 to 10 MPa·m$^{1/2}$. The fatigue precracking conditions are summarized for each specimen in **Appendix A**. The actual testing was performed according to ASTM E 740 in either ambient conditions (room temperature or RT), liquid nitrogen (LN2 or 76 K), or liquid helium (LHe or 4 K). The test machine had a load capacity of 1 MN and the maximum load was determined from the output of an x-y recorder. The dimensions of the specimens were measured with a shadowgraph at a magnification of 50x. The estimated accuracy of the residual strength measurement is ±1%.

RESULTS

<u>Alloy 2090 extrusions</u>:

The fracture test results for the extrusions are shown in **Table B3**. Little plasticity or stable crack growth was observed during testing of the extrusions so that the assumptions made in the calculcation of fracture toughness are valid. The residual strength at the three test temperatures vs. normalized flaw size is plotted in **Fig. B1**. As the test temperature goes down, the residual strength of the cracked panels remains approximately the same.

Figure B2 shows the fractography of the extrusions at room temperature. Macro-scopically, the fracture surface is smooth with no significant delaminations. At higher magnification, the surface is intergranular. As the test temperature decreases, there is little change in the fracture appearance.

32

Table B3a. Results for Alloy 2090 extrusions, large specimens (Type A).

ID	a^*, mm	$2c^*$, mm	t, mm	a/ϕ^{2*}, mm	Residual strength, MPa	Toughness, MPa·m$^{1/2}$
A1-RT	3.87	19.97	4.10	2.96	187	28.6
A2-RT	3.74	19.95	4.08	2.90	220	33.7
A3-LN2	2.93	20.32	4.08	2.47	231	32.7
A4-LN2	2.85	19.53	4.10	2.39	257	35.2
A5-LHe	2.84	19.41	4.05	2.38	281	38.5
A6-LHe	2.75	20.25	4.05	2.35	267	36.7

* defined in ASTM E 740.

Table B3b. Results for Alloy 2090 extrusions, small specimens (Type B).

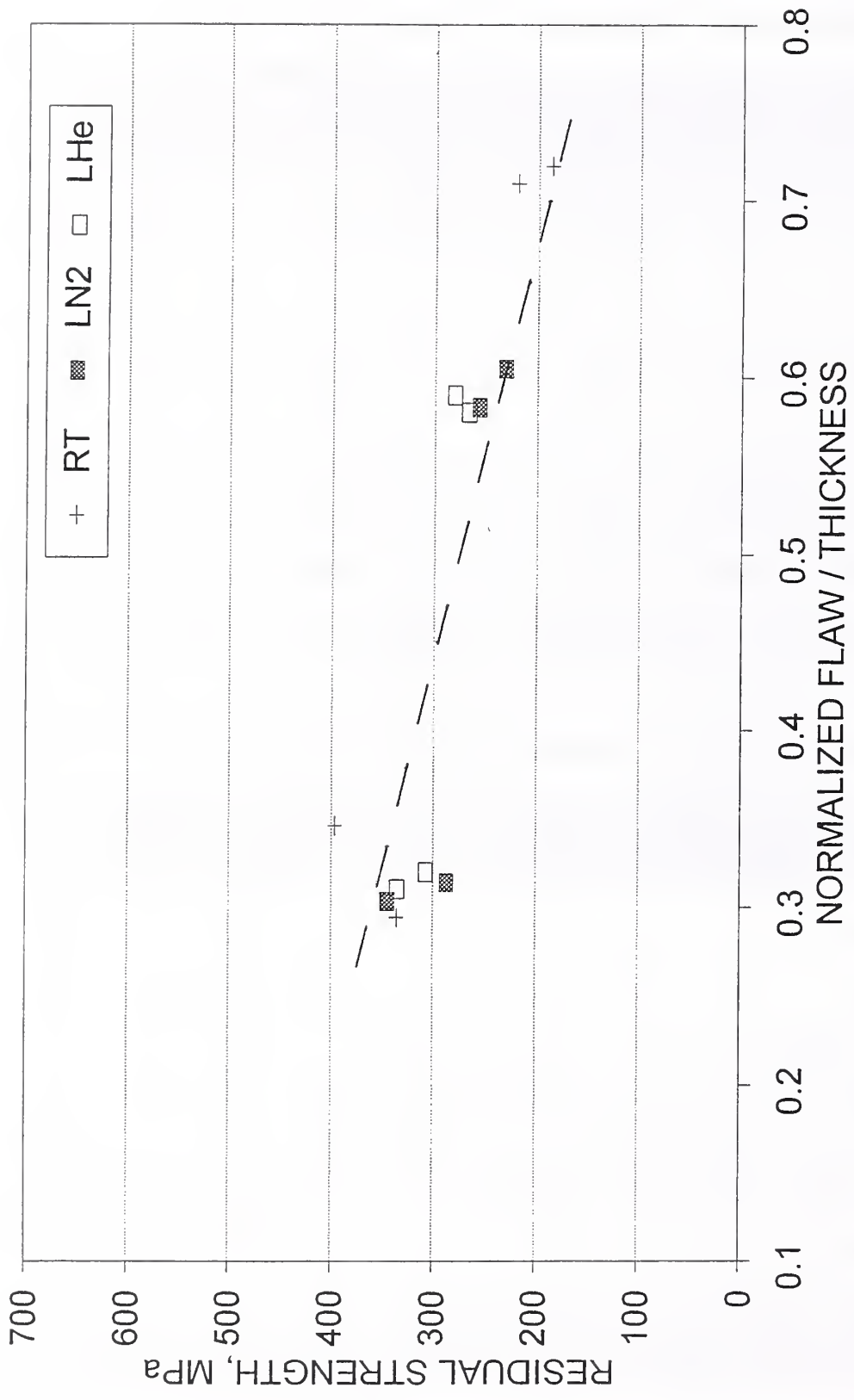| ID	a, mm	$2c$, mm	t, mm	a/ϕ^2, mm	Residual strength, MPa	Toughness, MPa·m$^{1/2}$
B1-RT	2.62	7.44	4.16	1.44	397	32.0
B2-RT	2.44	5.97	4.05	1.19	336	23.6
B3-LN2	2.44	6.18	4.03	1.22	346	24.9
B4-LN2	2.41	6.46	4.05	1.27	287	21.2
B5-LHe	2.84	6.46	4.05	1.30	308	22.8
B6-LHe	2.41	6.34	4.08	1.25	336	24.5

Fig. B1. Plot of residual strength vs. normalized flaw size for the extrusions from alloy 2090 as a function of test temperature.
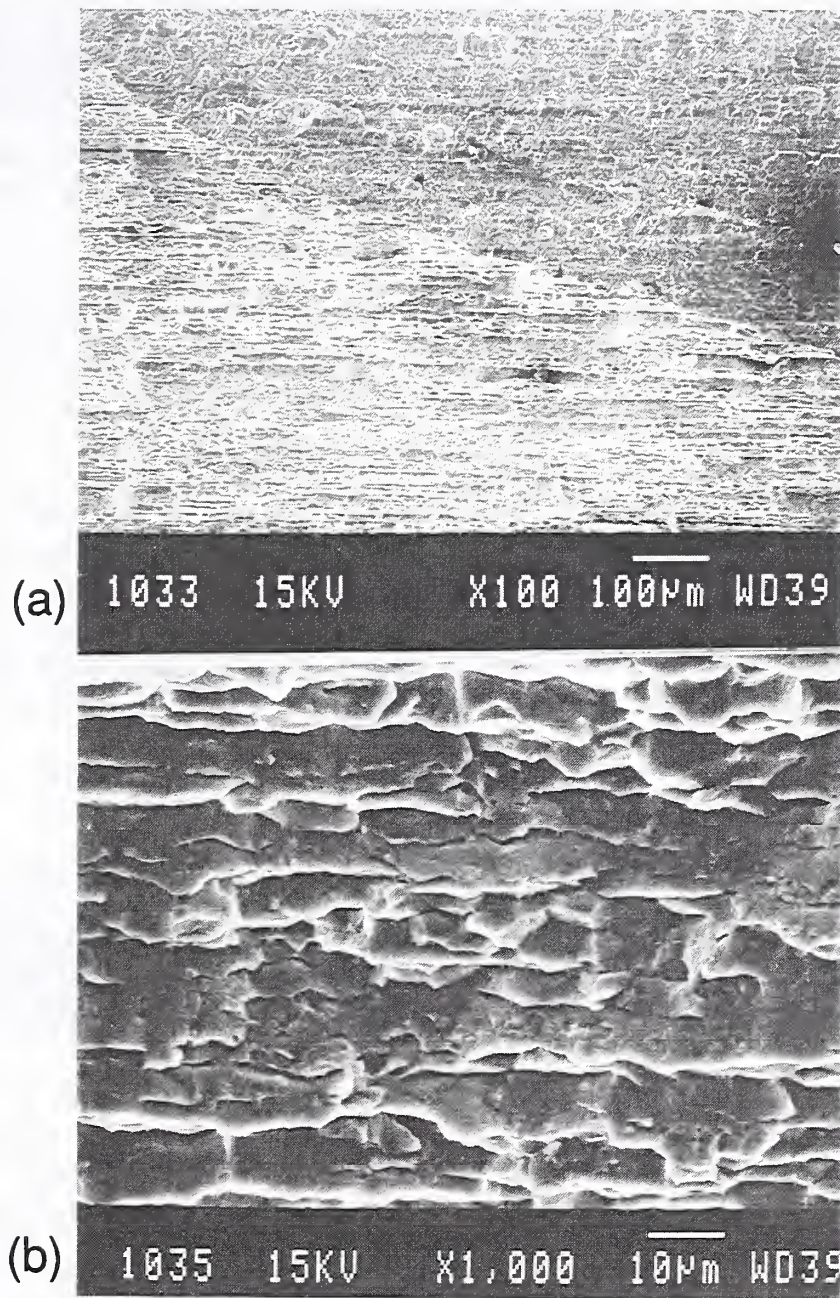
Fig. B2.   Fractographs from the surface of extruded specimen tested at room
temperature. (a) low magnification and (b) high magnification.

<u>Alloy 2090-T83 sheet</u>:

The results from the two sheets are shown in **Tables B4 and B5**. Little plasticity or stable crack growth was observed during testing of the extrusions so that the assumptions made in the calculation of fracture toughness are valid. At room temperature, the first lot has a slightly lower toughness and residual strength than the second sheet. For the second lot (**Table B5**), residual strength vs. normalized flaw size is plotted as a function of test temperature in **Fig. B3**. As the temperature goes down, the strength of the cracked panels from the second lot increases.

The appearances of fractured specimens from the two lots were quite different. The appearance of specimens from the first lot was relatively flat and exhibited no delaminations on the fracture surface, similar to the appearance of the extrusions, typical of that for a recrystallized microstructure.

Figure B4 shows fractography of the second lot. Delaminations were observed at both room and cryogenic temperatures, typical of that for a non-recrystallized micro-structure. The delaminations give the fracture surface a rough appearance by breaking the surface into several steps. The delaminations at cryogenic temperatures where often 3 mm steps on the fracture surface. At room temperature, the largest steps were about 1 mm.

Table B4. Results for Alloy 2090 sheet specimens from first lot.

ID	a, mm	$2c$, mm	t, mm	a/ϕ^2, mm	Residual strength, MPa	Toughness, MPa·m$^{1/2}$
B1-RT	2.46	5.92	4.34	1.18	398	27.5
B2-RT	2.51	6.15	4.36	1.23	356	25.3
B3-RT	2.69	6.00	4.35	1.21	342	23.8
A1-RT	4.35	20.26	4.40	3.19	227	31.7
A2-RT	4.25	19.72	4.28	3.12	250	34.3

Table B5a. Results for Alloy 2090 sheet specimens (Type A) from second lot.

ID	a, mm	2c, mm	t, mm	a/ϕ^2, mm	Residual strength, MPa	Toughness, MPa·m$^{1/2}$
A1-RT	2.36	20.00	4.35	2.08	351	42.3
A2-RT	3.08	20.00	4.32	2.54	360	50.6
A3-LN2[*]	---	---	---	---	---	---
A4-LN2	1.91	19.53	4.23	1.75	461	48.7
A5-LHe	1.84	19.41	4.31	1.68	518	52.8
A6-LHe	1.85	19.27	4.26	1.69	514	52.9

[*] Broke in grip section

Table B5b. Results for Alloy 2090 sheet specimens (Type B) from 2nd lot.

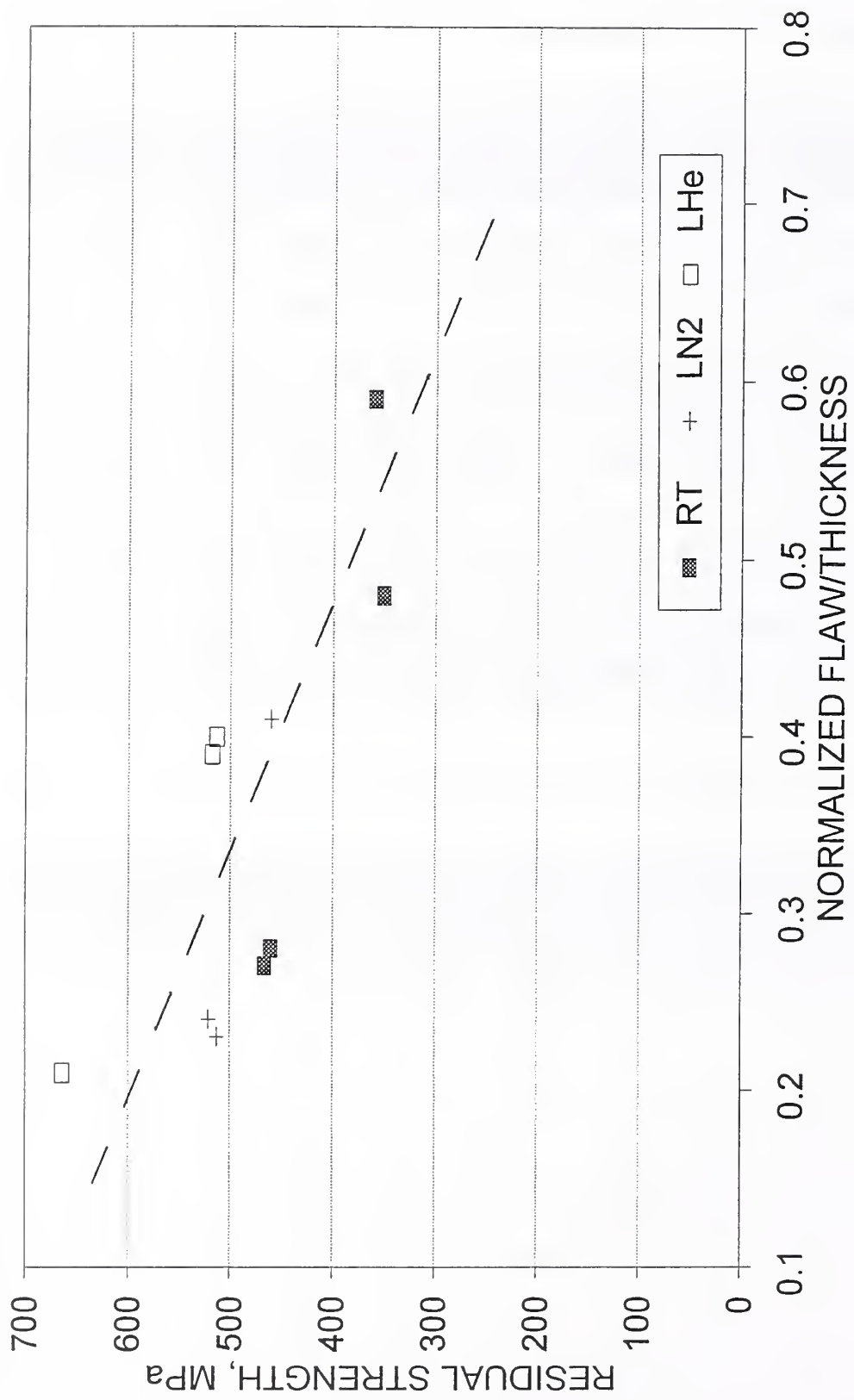| ID	a, mm	2c, mm	t, mm	a/ϕ^2, mm	Residual strength, MPa	Toughness, MPa·m$^{1/2}$
B1-RT	3.28	6.03	4.32	1.22	461	31.1
B2-RT	3.03	3.16	4.28	1.15	467	26.4
B3-LN2	2.51	5.00	4.26	1.01	521	32.1
B4-LN2	1.89	4.94	4.28	0.97	513	31.9
B5-LHe	2.12	4.32	4.26	0.88	664	37.7
B6-LHe[*]	---	---	---	---	---	---

[*] Broke in grip section.

Fig. B3.   Plot of residual strength vs. normalized flaw size for the second sheet of alloy 2090 as a function of test temperature.
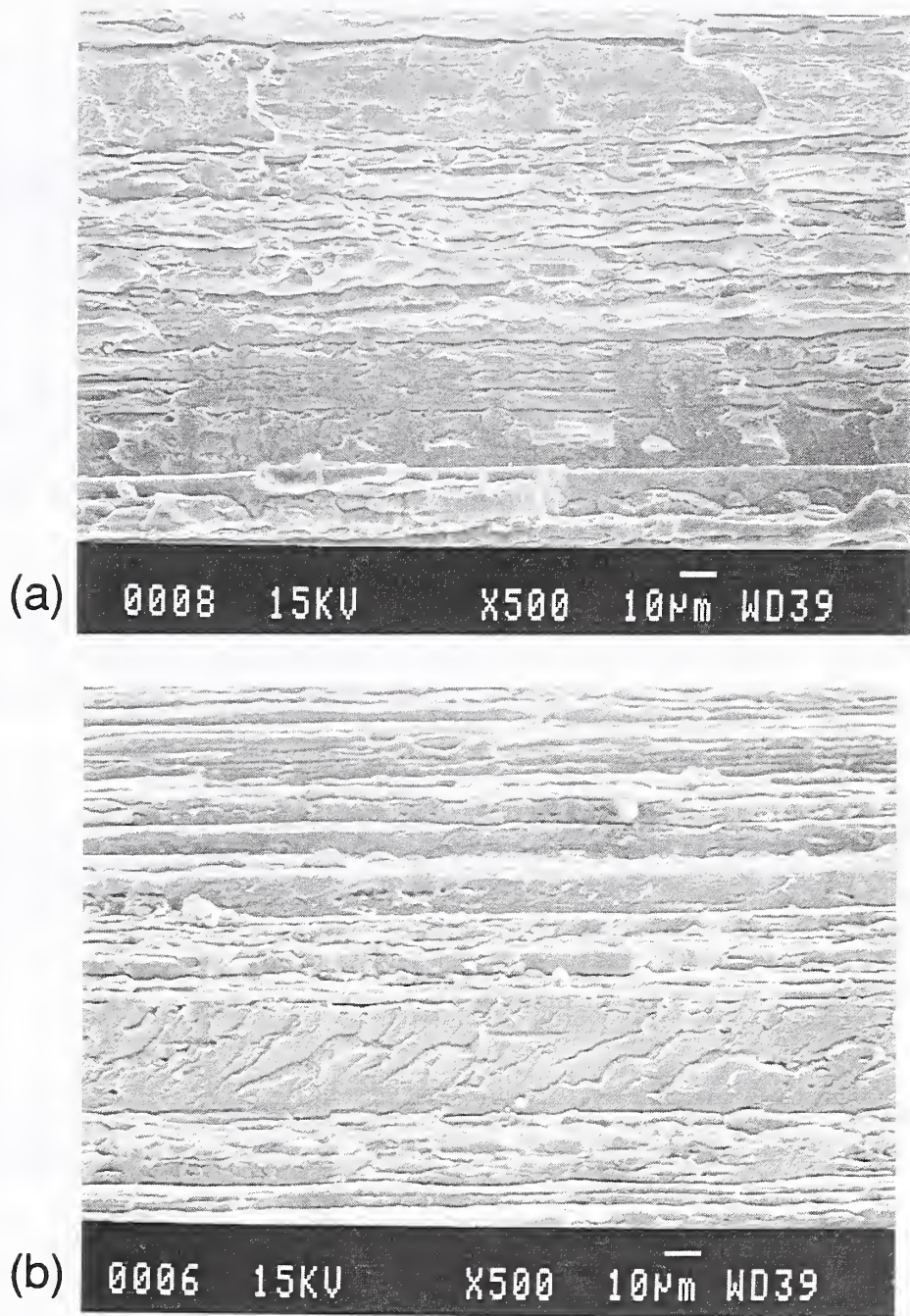
(a) 0008 15KV X500 10μm WD39

(b) 0006 15KV X500 10μm WD39

Fig. B4.   Fractographs from the surface of the delaminated sheet specimens (a) at RT and (b) at LN2 test temperature.

39

<u>Welds from Alloy 2090 extrusions:</u>

The results are shown in **Table B6**. During testing, significant nonlinear behavior was observed in the load-vs.-displacement. At room temperature, the deviation is due to plasticity at the crack tip; at cryogenic temperatures, the deviation is due to slow crack growth. In either case, the assumptions made in the calculation of fracture toughness are not valid. The residual strength vs. normalized flaw size is plotted in **Fig. B5**. The strength of the smaller flaws (normalized flaw of about 0.3 of the thickness) is about 50 MPa higher in LHe compared to that at RT. For larger flaws, the residual strength appears to be nearly the same under the two conditions.

The macroscopic fracture appearance depended upon test temperature. For specimens tested at RT, large shear lips are observed (indication of plane stress fracture mode) on the crack-side of the fracture surface. Yielding was apparent in the specimen and on the load-vs.-displacement curves before the maximum load was reached.

In LHe, no shear lips are present on the weld's fracture surface (sign of plane strain fracture). The load-vs.-displacement curves demonstrated large nonlinearity, but the nonlinearity was due to stable crack growth from the fatigue precrack rather than plasticity.

At higher magnification, the fracture appearance also depended upon test temperature. **Figure B6** shows the RT and LHe fracture surfaces of welded extrusions. The dominant fracture mechanism at RT (**Fig. B6a**) was dimpled rupture from second-phase particles. In LHe (**Fig. B6b**), the dominant fracture mechanism was intergranular with small secondary cracks present.

Table B6a. Results for Alloy 2090 welded extrusions, large specimens (Type A).

ID	a, mm	2c, mm	t, mm	a/ϕ^2, mm	Residual strength, MPa	TOUGHNESS,[*] MPa·m$^{1/2}$
Tested at RT						
W1-2/ W2-2	3.26	20.87	4.49	2.73	161	23.5
W3-1/ W5-1	2.62	19.26	4.28	2.26	191	24.6
Tested at LHe						
W4-1/ W5-2	2.65	19.71	4.36	2.29	208	27.0

[*] Validity requirements not met.

Table B6b. Results for Alloy 2090 welded extrusions, small specimens (Type B)

ID	a, mm	2c, mm	t, mm	a/ϕ^2, mm	Residual strength, MPa	Toughness,[*] MPa·m$^{1/2}$
Tested at RT						
W1-1/ W2-1	2.62	5.95	4.06	1.20	199	13.9
W3-1/ W5-1	2.35	5.78	4.15	1.16	216	14.7
Tested at LHe						
W4-1/ W5-2	3.08	6.53	4.28	1.34	257	18.8
W1-2/ W2-2	2.58	7.28	4.56	1.42	248	19.6

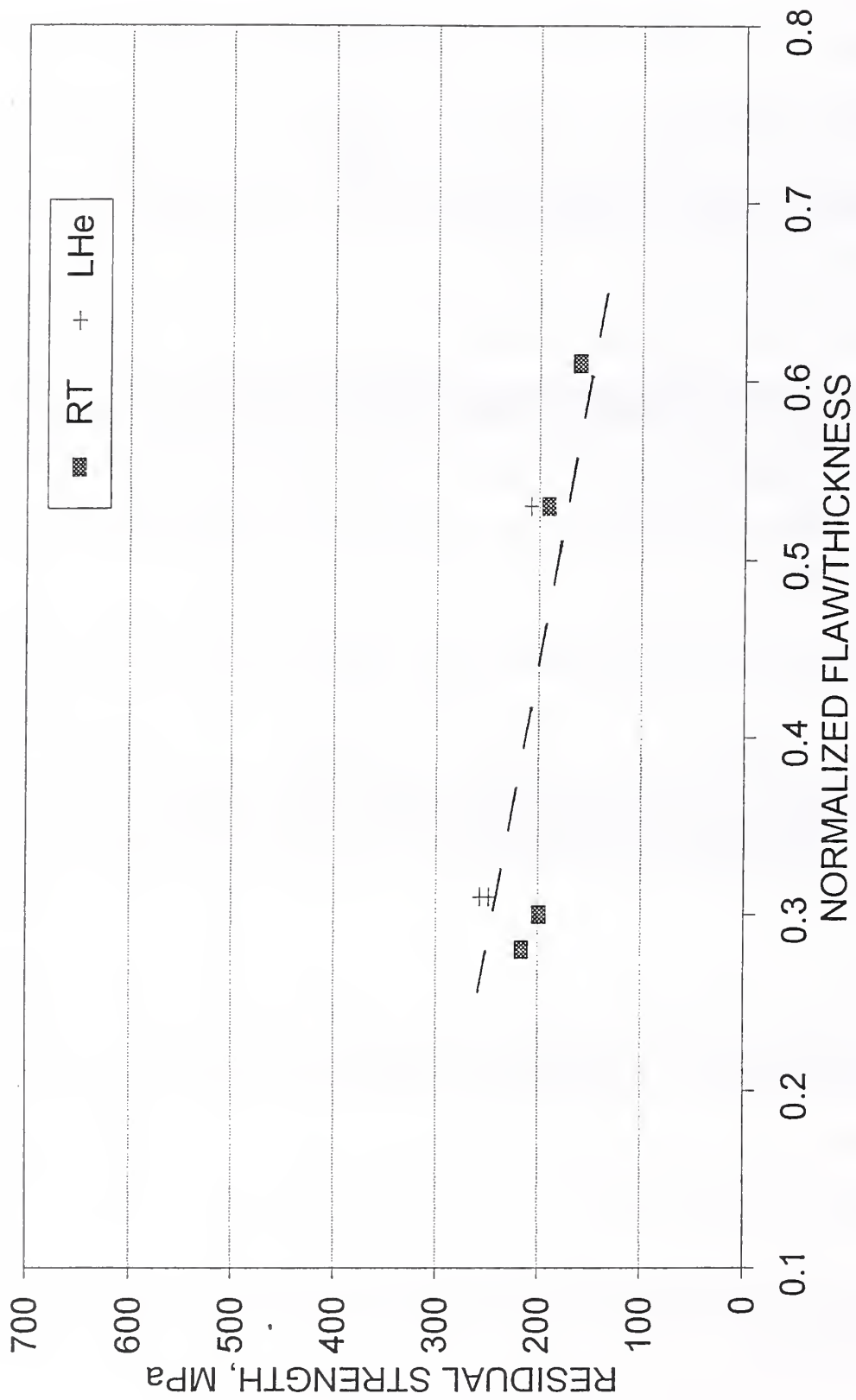[*] Validity requirements not met.

Fig. B5.   Plot of residual strength vs. normalized flaw size for the welds of alloy 2090 as a function of test temperature.
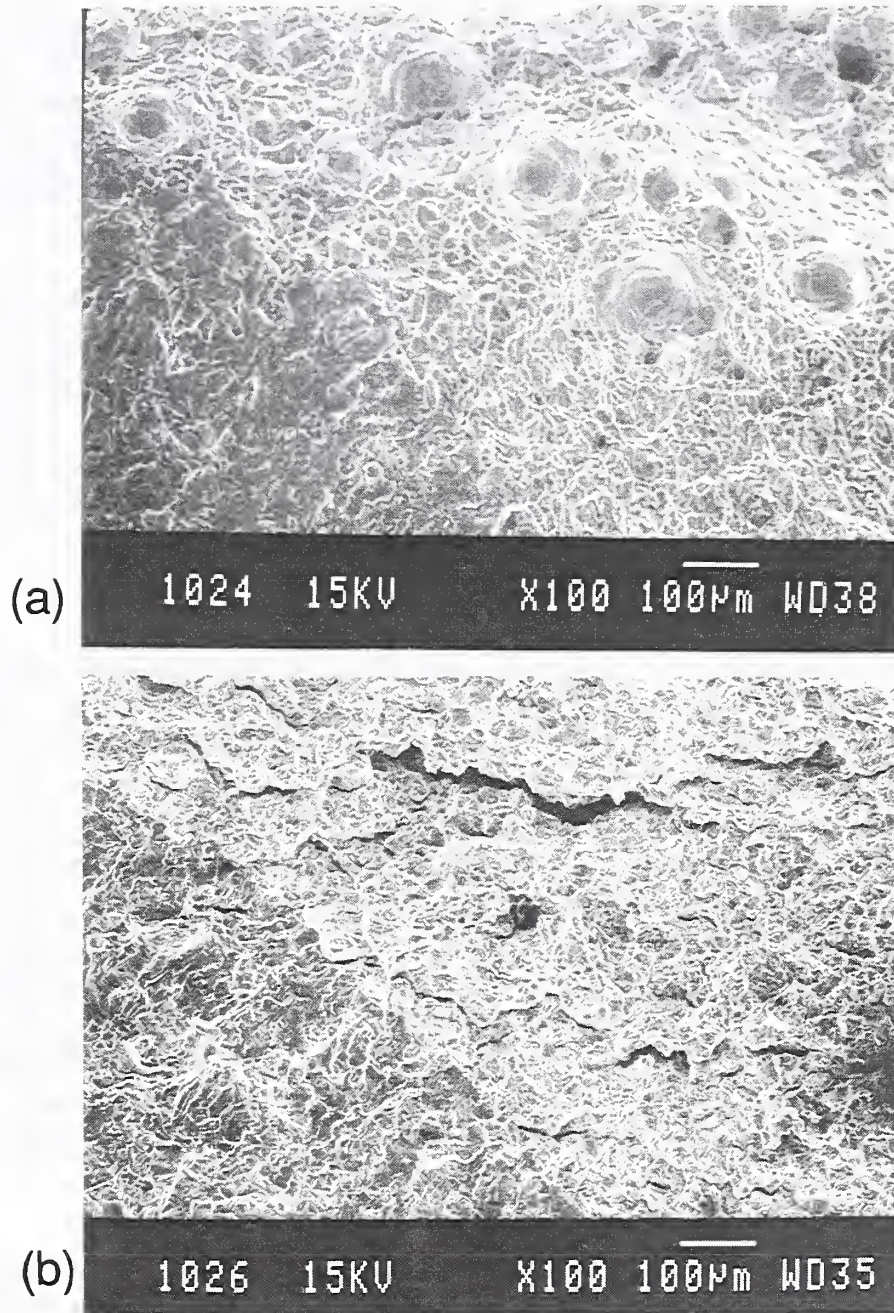
42

Fig. B6.   Fractographs from the surface of the welded specimens (a) at RT and (b) at LHe test temperature.

DISCUSSION

All the room-temperature tests from the four starting materials are shown in **Fig. 7**, a plot of residual strength vs. normalized flaw size. The second sheet of Alloy 2090, which displayed extensive delaminations, had the highest strength, followed by the extrusions, the first sheet of Alloy 2090, and then the welds, which exhibited the lowest strength. The difference between product forms is noticeable over the whole range of flaw sizes.

The most interesting result of this program is for the sheet product form. The two sheets tested in this program were produced to similar requirements and with similar chemical compositions, but were taken from different production lots. The results from the two sheets proved quite different. Take for example a comparison of Type B specimens (small flaws with a normalized flaw of about 25% of the thickness). The sheet that exhibited delaminations (B1-RT in **Table B5**) had a residual strength that was 100 MPa higher than the average strength of the three simliar specimens tested from the sheet that did not exhibit delaminations (B1,2,&3-RT in **Table B4**).

The temperature dependence of the residual strength is the most critical consideration for many aerospace applications [B2]. **Figure B8** shows a plot of the residual strength at different temperatures vs. normalized flaw size for Alloy 2090 sheet (lot 2) and one of the Alloy 2090 plates tested in the previous program (both exhibited significant delamination). In both cases, the residual strength increases as the test temperature decreases. The apparent "delamination toughening" of Alloy 2090 sheet and plate with decreasing test temperature contradicts the results reported by Tack and Loechel [B2]. There could be differences in the fatigue precracking prior to testing which could explain the contradiction. For the testing reported here, the tension-tension precracking was continued for about 20 000 cycles at a low stress intensity factor or until the fatigue zone was approximately 1 mm away from the EDM notches on the surface. If the fatigue crack growth on each side of the EDM notch were less than 1 mm and/or if the fatigue crack growth rate were faster, there might have been different results. The exact fatigue precracking conditions were not reported in [B2].

The low defect tolerance of the welds is not unusual and is typically compensated for by increasing the thickness of the weld lands, reducing the stress in the region. A promising area for future research would be to increase the strength and defect tolerance of the welds. One possible approach is plastically deforming the welded joint. This would certainly raise the strength. As far as toughness is concerned, the welds already behave in a brittle fashion at cryogenic temperatures (see **Fig. B6**, where the fracture mechanism changes from ductile rupture to intergranular).

Fig. B7. Plot of residual strength vs. normalized flaw size for different product
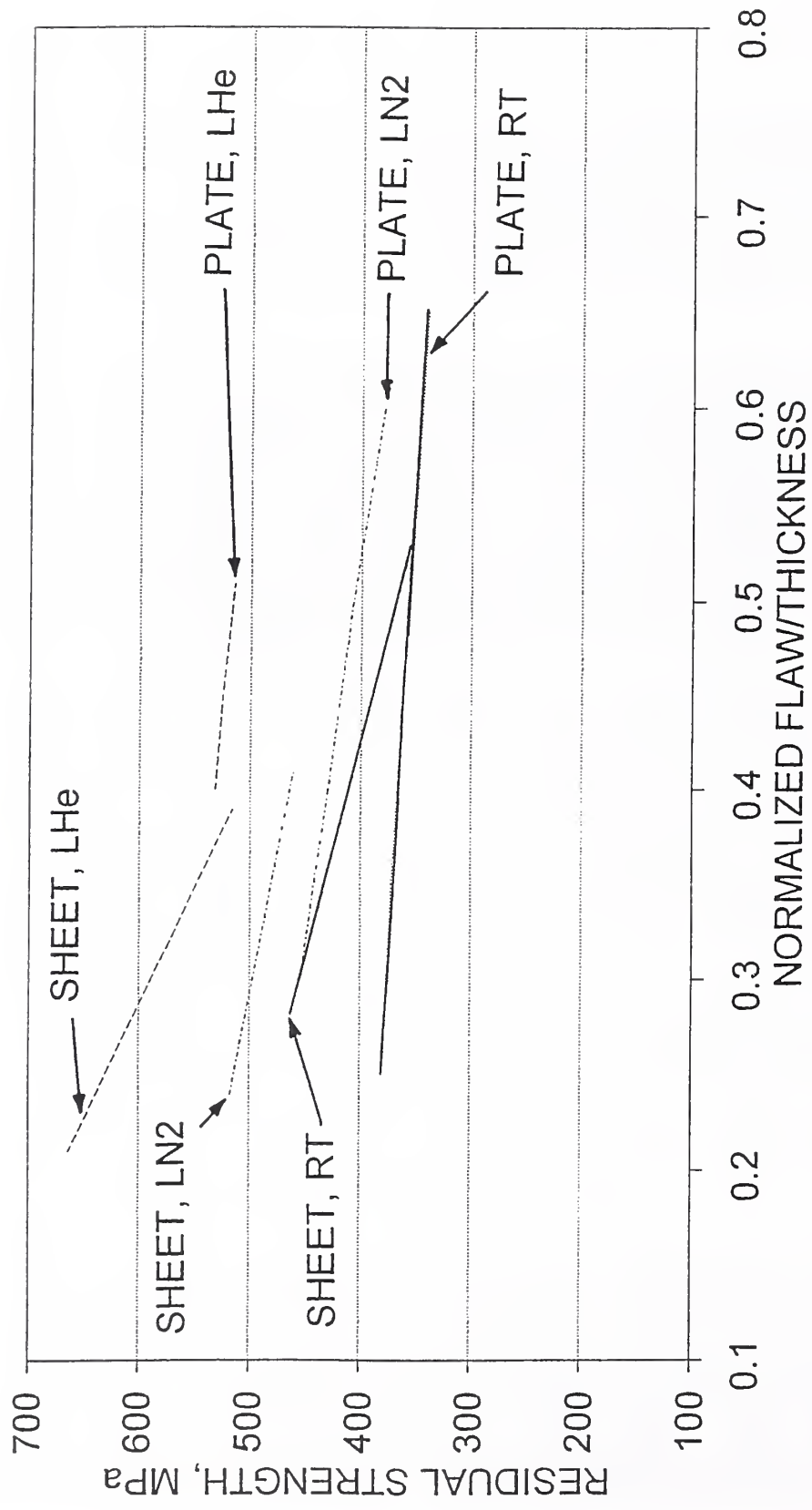forms for alloy 2090 at RT.

45

Fig. B8.   Plot of residual strength vs. normalized flaw size for alloy 2090 delaminated sheet and plate [B1] as a function of test temperature.

46

CONCLUSIONS

1. The sheet of Alloy 2090 that exhibited delaminations on the fracture surface had the higher defect tolerance than either the extrusions or welds. In addition, the defect tolerance at cryogenic temperatures increased over that at room temperature.

2. The superior performance of sheets is attributed to toughening due to the formation of delaminations on the fracture surface.

3. The extrusions from Alloy 2090 exhibit a nearly constant defect tolerance at cryogenic temperatures compared to room temperature. No delaminations were observed on the fracture surface of the extrusions at any test temperature. At room temperature, the defect tolerance of the extrusions was similar to that of a sheet of Alloy 2090 which did not exhibit delaminations.

4. The welds from Alloy 2090 extrusions exhibited the lowest defect tolerance of any of the product forms tested to date, roughly half that found for the sheet that exhibited delaminations. For smaller flaws, the defect tolerance at 4 K is about 25% greater than at room temperature. For larger flaws, the residual strength was approximately the same at both temperatures.

ACKNOWLEDGEMENTS

REFERENCES

B1. P.T. Purtscher, M. Austin, S. Kim, and D. Rule, "Aluminum-Lithium Alloys: Surface-Cracked Tension Fracture Tests and Physical and Thermal Properties at Cryogenic Temperatures", NISTIR 3986, National Institute of Standards and Technology, Boulder, CO, 1992.

B2. W.T. Tack and L.W. Loechel, in Aluminum-Lithium, eds. M. Peters and P.-J. Winkler, Informationsgesellschaft Verlag, Germany, 1992, pp. 415-420.

APPENDIX A

Table 1-A. Fatigue precracking information from the first sheet of Alloy 2090.

Specimen #	Load (kN)	# of cycles
A1-RT	53	38267
A2-RT	49	54167
B1-RT	38	52893
B2-RT	38	32961
B3-RT	38	23917

Table 2-A. Fatigue precracking information from the second sheet of Alloy 2090.

Specimen #	Load (kN)	# of cycles
A1-RT	2[*] 44	51610 11096
A2-RT	67	42222
A3-LN2	49	25200
A4-LN2	76	34232
A6-LHe	76	30167
A6-LHe	76	28340
B1-RT	53	51793
B2-RT	53	46202
B3-LN2	62	20045
B3-LN2	62	22827
B5-LHe	62	25200
B6-LHe	62	22112

[*] DENOTES three-point bending WITH SPAN OF 100 mm

48

Table 3-A. Fatigue precracking data from the extrusions of Alloy 2090.

Specimen #	Load (kN)	# of cycles
A1-RT	31	35610
A2-RT	1.5* 49	16800 7000
A3-LN2	1.5* 40	26580 2000
A3-LN2	1.5* 40	36110 2000
A5-LHe	1.5* 40	22640 2000
A6-LHe	1.5* 40	24280 2000
B1-RT	53	23896
B2-RT	31	27342
B3-LN2	36	24303
B4-LN2	36	22607
B5-LHe	36	19063
B6-LHe	36	21379

* Denotes three-point bending with a span of 100 mm

Table 4-A. Fatigue precracking information from the welds of Alloy 2090.

Specimen #	Load (kN)	# of cycles
A/ W1-1/W2-1	1.5* 22	28826 2500
A/ W1-2/W2-2	1.5* 22	45499 2205
A/ W3-1/W5-1	1.5* 22	46919 2505
A/ W5-2/W4-1	1.5* 22	28211 2005
B/ W1-1/W2-1	31	14176
B/ W1-2/W2-2	22	68295
B/ W3-1/W5-1	20	129300
B/ W5-2/W4-1	22	325937

* Denotes three-point bending with a span of 100 mm